Monthly Notices
of the
ROYAL ASTRONOMICAL SOCIETY

Mon. Not. R. Astron. Soc. **421,** 1874–1890 (2012) doi:10.1111/j.1365-2966.2012.20195.x

Prompt, early and afterglow optical observations of five γ-ray bursts: GRB 100901A, GRB 100902A, GRB 100905A, GRB 100906A and GRB 101020A

E. S. Gorbovskoy,[1⋆] G. V. Lipunova,[1⋆] V. M. Lipunov,[1] V. G. Kornilov,[1] A. A. Belinski,[1] N. I. Shatskiy,[1] N. V. Tyurina,[1] D. A. Kuvshinov,[1] P. V. Balanutsa,[1] V. V. Chazov,[1] A. Kuznetsov,[1] D. S. Zimnukhov,[1] M. V. Kornilov,[1] A. V. Sankovich,[1] A. Krylov,[1] K. I. Ivanov,[2] O. Chvalaev,[2] V. A. Poleschuk,[2] E. N. Konstantinov,[2] O. A. Gress,[2] S. A. Yazev,[2] N. M. Budnev,[2] V. V. Krushinski,[3] I. S. Zalozhnich,[3] A. A. Popov,[3] A. G. Tlatov,[4] A. V. Parhomenko,[4] D. V. Dormidontov,[4] V. Senik,[4] V. V. Yurkov,[5] Yu. P. Sergienko,[5] D. Varda,[5] I. P. Kudelina,[5] A. J. Castro-Tirado,[6] J. Gorosabel,[6] R. Sánchez-Ramírez,[6] M. Jelinek[6] and J. C. Tello[6]

[1]*Moscow MV Lomonosov State University, Sternberg Astronomical Institute, Moscow 119992, Russia*
[2]*Irkutsk State University, ul. Karla Marxa 1, Irkutsk 664003, Russia*
[3]*Kourovka Astronomical Observatory, Physical Department of Ural State University, pr. Lenina 51, Ekaterinburg 620083, Russia*
[4]*Kislovodsk Solar Station of the Pulkovo Observatory RAS, PO Box 45, ul. Gagarina 100, Kislovodsk 357700, Russia*
[5]*Blagoveschensk State Pedagogical University, ul. Lenina 104, Amur Region, Blagoveschensk 675000, Russia*
[6]*Instituto de Astrofísica de Andalucía (IAA-CSIC), Glorieta de la Astronomía s/n, 18008 Granada, Spain*

Accepted 2011 November 13. Received 2011 November 2; in original form 2011 June 24

ABSTRACT

We present the results of the prompt, early and afterglow optical observations of five γ-ray bursts (GRBs): GRB 100901A, GRB 100902A, GRB 100905A, GRB 100906A and GRB 101020A. These observations were made with the Mobile Astronomical System of TElescope-Robots in Russia (MASTER-II Net), the 1.5-m telescope of the Sierra Nevada Observatory and the 2.56-m Nordic Optical Telescope. For two sources, GRB 100901A and GRB 100906A, we detected optical counterparts and obtained light curves starting before the cessation of γ-ray emission, at 113 and 48 s after the trigger, respectively. Observations of GRB 100906A were conducted in two polarizing filters. Observations of the other three bursts gave the upper limits on the optical flux; their properties are briefly discussed. A more detailed analysis of GRB 100901A and GRB 100906A, supplemented by *Swift* data, provides the following results and indicates different origins for the prompt optical radiation in the two bursts. The light-curve patterns and spectral distributions suggest that there is a common production site for the prompt optical and high-energy emission in GRB 100901A. The results of the spectral fits for GRB 100901A in the range from optical to X-ray favour power-law energy distributions and a consistent value of the optical extinction in the host galaxy. GRB 100906A produced a smoothly peaking optical light curve, suggesting that the prompt optical radiation in this GRB originated in a front shock. This is supported by a spectral analysis. We have found that the Amati and Ghirlanda relations are satisfied for GRB 100906A. We obtain an upper limit on the value of the optical extinction on the host of GRB 100906A.

Key words: telescopes – gamma-ray burst: general – gamma-ray burst: individual: GRB 100901A – gamma-ray burst: individual: GRB 100906A.

⋆E-mail: gorbovskoy@sai.msu.ru (ESG); galja@sai.msu.ru (GVL)

1 INTRODUCTION

Since 1997, when the optical radiation of γ-ray bursts (GRBs) was first detected, we have known that these are the most energetic events in the Universe (Kulkarni et al. 1998). Optical emission that is observed hours after a GRB is attributed to the so-called afterglow, which is the result of a shock propagating outward in the surrounding media (Mészáros & Rees 1997). The characteristics of such an emission are defined mainly by conditions in the interstellar medium (ISM) and the amount of released energy, but they depend weakly on the details of the central burst.

The nature of GRBs and their emission mechanisms are not completely understood, and more observational data and model analysis are necessary for further understanding. An acknowledged model is that a GRB is a manifestation of the formation of a rotating black hole (or another compact relativistic object) in the course of gravitational collapse. An engine converts the energy of the collapse into emissions of different types, among which there is a high-energy γ emission that is produced for up to several tens of seconds. The afterglow emission is detected long afterwards, whether the engine is still working or not, which is uncertain. In order to better understand the details of the process, it is necessary to observe the main event itself, at different wavebands, while the engine is at its most active stage.

However, it is a challenge to observe prompt optical emission because a GRB usually lasts no more than several tens of seconds. Although the prompt optical observations of GRBs were first carried out in 1998 by Akerlof et al. (2000), successful prompt optical detections remain rare. Evidently, there are two approaches: to observe extensive sky fields and wait for a GRB to occur or to use special robotic telescopes that can be ready to point anywhere with an alert from an orbital γ-ray observatory (the 'alert observations' technique). The Mobile Astronomical System of TElescope-Robots in Russia (MASTER-II[1]) uses both techniques (Lipunov et al. 2010). Our paper is dedicated to the alert MASTER observations of five GRBs in Siberia, Ural and North Caucasus.

Alert ground-based optical observations of GRBs are a new global physical experiment, which have been available since the last decade. They are made possible because of the implementation of the global Internet network, powerful personal computers and fast optical CCD receivers. The challenge is to quickly accomplish the four following steps as early as possible.

(i) A GRB is detected by a γ-ray telescope on board a spacecraft, such as *Swift* (Gehrels et al. 2004), *Fermi* (Atwood et al. 2009), *INTEGRAL* (Winkler et al. 2003), etc.

(ii) After the onboard processing is finished, the location of a GRB is sent to the GRB Coordinates Network (GCN) at the National Aeronautics Space Administration (NASA). The first two steps take 10–40 s.

(iii) The burst position is then disseminated to ground-based robotic telescopes through the Internet network (in about 0.5 s).

(iv) The robotic telescopes are scheduled and pointed to the received positions, which takes 7–40 s for moderate-size instruments (less than 0.5 m) and from several minutes to hours for 2-m and larger instruments. Whereupon, imaging is performed in the optical and infrared bands.

The first Russian robotic telescope MASTER came into operation in 2002 near Moscow, with the help of private funding from the Moscow association Optics.[2] Construction of the all-Russia network MASTER began in 2008 (Lipunov et al. 2010). At present, the telescopes of the MASTER-Net are located in the observatories of Moscow State University (in Kislovodsk), Ural State University (in Kourovka), Irkutsk State University (in Tunka near Baikal Lake) and the Blagoveschensk Pedagogical University (in the Blagoveschensk region). These observatories span six time zones. A description of the MASTER II telescopes can be found in Kornilov et al. (2011).

In 2010 September and October, the MASTER telescopes made five target observations of GRBs that triggered the *Swift* observatory: GRB 100901A, GRB 100902A, GRB 100905A, GRB 100906A and GRB 101020A. Here, we report on these observations and make an analysis for two long GRBs, whose counterparts were successfully detected. For one of these, GRB 100906A, we also use the data obtained with the 1.5-m telescope at the Sierra Nevada Observatory (OSN) and the 2.56-m Nordic Optical Telescope (NOT). We begin in Section 2 with a description of the observations. We describe the reduction and analysis of the data obtained by MASTER in Section 3, and we also describe the preparation of the *Swift* light curves and spectra from the data available on-line. In Section 4, we discuss the results for GRB 100901A and GRB 100906A, including the spectra before T_{90}, the late-time spectra, the estimates of the optical extinction in the host galaxies and the search for the jet break time on the light curve of GRB 100906A after 10 000 s. In Section 5, we consider the arguments concerning the different sites for the prompt optical emission in GRB 100901A and GRB 100906A. We also discuss their spectral evolution, and the spectral characteristics of other GRBs, for which optical counterparts were not detected. We check the applicability of the Amati and Ghirlanda relations to GRB 100901A and GRB 100906A. We also mention the model of two-step collapse for the long engine activity, which can cause a bump on the X-ray and optical light curves of GRB 100901A. We summarize our results in Section 6.

Throughout this paper, we adopt a standard CDM cosmology with $H_0 = 70$ km s^{-1} Mpc^{-1}, $\Omega_{\rm m} = 0.27$ and $\Omega_\Lambda = 0.73$. We define the flux density power-law temporal and spectral decay indices as $F_\nu \propto t^{-\alpha}\nu^{-\beta}$, and the photon index equals $\beta + 1$. All errors in the paper are 1σ uncertainties unless otherwise noted. All *Swift* data used to reproduce the light curves and spectra were taken from the *Swift* catalogue,[3] the UK *Swift* data archive[4] and the Burst Analyser website.[5]

2 OBSERVATIONS

At present, the MASTER-II Net consists of four identical, fast telescopes located at different sites in Russia (Lipunov et al. 2010; Kornilov et al. 2011). Each telescope is a twin-tube instrument with an aperture of 0.4 m and a focal ratio $f/2.5$. Each telescope is equipped with a CCD camera 4 × 4 K AltaU-16M, providing a field of view of 2×2 deg^2. A photometric unit provides a set of four filters, which can be placed in turn at the optical axis before the CCD camera. Depending on the long-term scientific task, the photometric units of the twin telescopes are supplied with three filters (any of the following: Johnson B, V, R, I and white glass).

[1] The MASTER web site is http://observ.pereplet.ru.

[2] http://www.ochkarik.ru/master/

[3] http://heasarc.nasa.gov/docs/swift/archive/grb_table/

[4] http://www.swift.ac.uk/swift_portal/

[5] http://www.swift.ac.uk/burst_analyser/

The fourth position is occupied by polarization filters, oriented orthogonally in the two tubes. Polarization filters are positioned differently in the celestial coordinate system at the telescopes of the MASTER-Net.

Each observatory operates automatically. Waiting for an alert signal, MASTER II monitors the sky searching for possible optical transients. Swapping from the monitoring to alert observations of GRBs is accomplished by switching the filters, focusing and pointing the telescope to the event coordinates received from the GCN. Within 20 s after an alert, the MASTER II observatory is ready to observe a GRB. The pointings at the positions of the GRBs considered here took 22–47 s.

2.1 Prompt optical observations of GRB 100901A

GRB 100901A triggered the *Swift*/Burst Alert Telescope (BAT) at 13:34:10 UT on 2010 September 1. The time T_{90}, during which 90 per cent of γ fluence is detected, was 439 ± 33 s (Immler et al. 2010; Sakamoto et al. 2010b).

Two MASTER robotic telescopes were pointed to the *Swift*/BAT position of GRB 100901A: at Tunka, 103 s after the BAT trigger time $T0$, and near Blagoveschensk, 101 s after $T0$ (Ivanov et al. 2010a). We have obtained more than ∼5 min of optical observations simultaneous to the prompt γ emission of the GRB. The source was not far enough above the horizon at Tunka, and it was only possible to observe it with one of the optical tubes. The second tube was shadowed by the dome, which made it impossible to measure the polarized light. The eastern telescope, near Blagoveschensk, was not operational because of bad weather conditions. An optical flare, with a maximum at 17.0 mag in the MASTER unfiltered band, was clearly detected at 426 ± 40 s after the trigger time (Ivanov et al. 2010b), synchronously with the X-ray flare (Page & Immler 2010) and the γ flare (Sakamoto et al. 2010b).

The MASTER telescope at Kourovka was pointed to GRB 100901A ∼5 h later. Overall, we continuously observed the GRB for 14 h at three sites (Tunka, Kourovka and Kislovodsk), in different optical bands: unfiltered, R, I and V. The resulting data are summarized in Table 1 and are presented in Figs 1 and 2. Fig. 1 also shows *Swift*/X-ray Telescope (XRT) 0.3–10 keV and *Swift*/BAT 15–350 keV light curves for GRB 100901A (for a description, see Section 3.3).

The OSN observed the GRB about 11 h after the trigger (Sanchez-Ramirez et al. 2010). The redshift of the host galaxy $z = 1.408$ was obtained at the 8-m Gemini North telescope (Chornock et al. 2010).

2.2 Prompt optical observations of GRB 100902A

On 2010 September 2, the Kourovka MASTER telescope was pointed to the BAT position of GRB 100902A (Sakamoto et al. 2010c), 104 s after the GRB trigger time $T0$ 19:31:54 UT. This GRB flaring activity lasted for about 200 s after the trigger time, and MASTER was first to witness its active stage in the optical waveband. The imaging was attempted at two polarization angles, with 20-s exposure times. However, no optical transient was found at the XRT position with the upper limit of 17 mag (Krushinski et al. 2010a). The final results of our photometry (Gorbovskoy et al. 2010), which are the upper limits on the optical flux at two polarization angles, are summarized in Table 2. The GRB position was observed by the OSN ∼7 h after the trigger with an upper limit on the magnitude in the I band: ∼21.8 mag (Tello et al. 2010).

2.3 Early optical observations of GRB 100905A

On 2010 September 5, a GRB was detected by *Swift*/BAT at 15:08:15 UT (Marshall et al. 2010). The Tunka MASTER telescope was pointed to its position 55 s after $T0$. The imaging was carried out at two polarization angles (Ivanov et al. 2010c). No optical transient was found. The upper limits are given in Table 3. Further optical observations were carried out by the *Swift*/Ultraviolet/Optical Telescope (UVOT) (Siegel & Marshall 2010) and the 1.5-m telescope of the OSN (Sota, de Ugarte Postigo & Castro-Tirado 2010). These did not yield an optical counterpart either. Barthelmy et al. (2010a) found that $T_{90} = 3.4 \pm 0.5$ s, which implies that our observations can be qualified as 'early', not prompt. This γ-ray burst might belong to the class of intermediate duration GRBs, separated from the class of long GRBs on statistical grounds by Horváth (1998, 2002) and Mukherjee et al. (1998). While the underlying physical properties of the subclasses of long GRBs appear to be similar (type of progenitor, interstellar environment), there is evidence for duration and luminosity differences caused by some slight diversity of the bursts (de Ugarte Postigo et al. 2011).

2.4 Prompt and afterglow optical observations of GRB 100906A

At 13:49:27 UT on 2010 September 6, GRB 100906A was detected (Markwardt et al. 2010). The *Swift*/BAT detected several bright peaks with $T_{90} = 114.4 \pm 1.6$ s (Barthelmy et al. 2010b). GRB 100906A has been also observed by the Konus–*Wind* starting from 13:49:30 UT (Golenetskii et al. 2010).

Table 1. Photometry of GRB 100901A by MASTER: R, unfiltered W, I and V. Times $t - T0$ are the middle times of the exposures, which are listed in columns 2, 5, 8 and 11. This is a sample of the full table, which is available as Supporting Information with the electronic version of the article.

$t - T0$ (h)	Exp. (s)	R (mag)	$t - T0$ (h)	Exp. (s)	W (mag)	$t - T0$ (h)	Exp. (s)	I (mag)	$t - T0$ (h)	Exp. (s)	V (mag)
4.1381	180	18.08 ± 0.45	0.0315	20	18.93 ± 2.00	5.4149	180	17.00 ± 0.09	0.3811	180	17.96 ± 0.19
4.3939	180	17.81 ± 0.17	0.0426	30	18.23 ± 0.80	5.4719	180	16.96 ± 0.09	0.5449	180	17.96 ± 0.19
4.4545	180	17.56 ± 0.11	0.0591	40	18.42 ± 0.80	5.5288	180	17.07 ± 0.10	0.6021	180	17.76 ± 0.17
4.5129	180	17.61 ± 0.10	0.0950	60	18.53 ± 0.70	5.5857	180	16.87 ± 0.08	5.5865	180	17.59 ± 0.11
4.5705	180	17.45 ± 0.08	0.1185	80	17.51 ± 0.25	5.6426	180	17.04 ± 0.09	5.6451	180	17.70 ± 0.12
4.6278	180	17.77 ± 0.10	0.1475	100	18.47 ± 0.50	5.6999	180	17.04 ± 0.09	7.1125	180	17.92 ± 0.18
4.6857	180	17.33 ± 0.07	0.1820	120	18.85 ± 0.70	5.7568	180	17.05 ± 0.09	7.1718	180	17.79 ± 0.15
4.7428	180	17.56 ± 0.09	0.2233	150	18.62 ± 0.60	5.8138	180	16.83 ± 0.07			
4.8000	180	17.45 ± 0.07	0.2732	180	17.94 ± 0.30	5.8706	180	16.81 ± 0.07			
4.8571	180	17.39 ± 0.07	0.3272	180	17.99 ± 0.30	5.9277	180	16.92 ± 0.07			

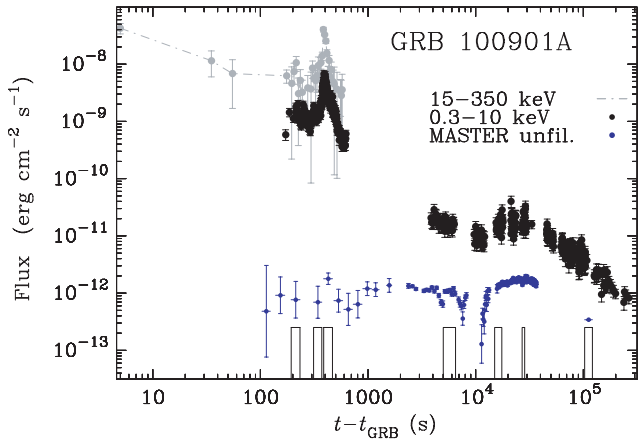

Figure 1. The optical light curve of GRB 100901A obtained by MASTER (blue points with vertical bars representing errors and horizontal bars representing exposure times; data are corrected for the Galactic extinction) along with the *Swift*/BAT 15–350 keV flux with 10-s binning (grey dots connected by dot-dashed lines) and *Swift*/XRT 0.3–10 keV unabsorbed flux (black dots; Page & Immler 2010). Thin-line rectangles show the time intervals selected for spectral analysis. Colour figures can be viewed in the electronic version.

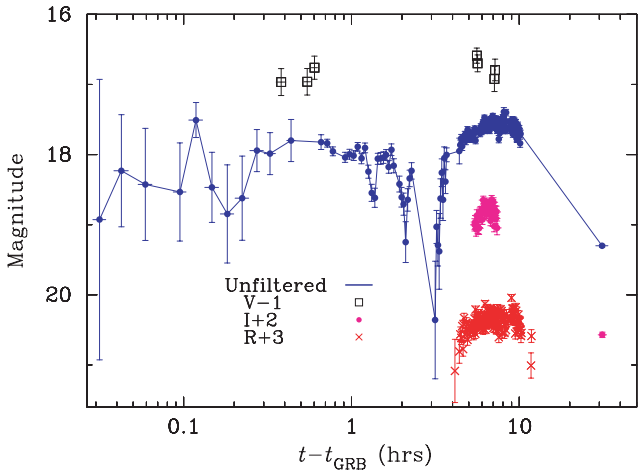

Figure 2. MASTER optical light curves of GRB 100901A in different filters: *R* (3 mag added; red crosses), *I* (2 mag added; magenta dots), *V* (1 mag subtracted; black squares) and unfiltered (blue dots connected with solid line). Magnitudes are not corrected for the Galactic extinction. Horizontal bars show exposures.

Table 2. MASTER upper limits on the optical flux obtained with the polarizing filter for GRB 100902A. The bottom row is co-added from all of the above exposures.

t_{start} (UT)	t_{end} (UT)	Exposure time (s)	$t_{start} - T0$ (s)	mag
19:33:38	19:33:58	20	104.0	17.0
19:34:12	19:34:42	30	132.0	17.3
19:34:57	19:35:57	40	177.0	17.3
19:35:51	19:36:41	50	231.0	17.4
19:33:38	19:36:41	140	104.0	18.0

Table 3. MASTER upper limits on the optical flux obtained with polarizing filter for GRB 100905A.

t_{start} (UT)	t_{end} (UT)	Exposure time (s)	$t_{start} - T0$ (s)	mag
15:09:10	15:09:20	10	55.0	16.5
15:09:39	19:09:59	20	84.0	17.1
15:10:45	15:11:15	30	150.0	17.3
15:11:35	15:12:15	40	200.0	17.5

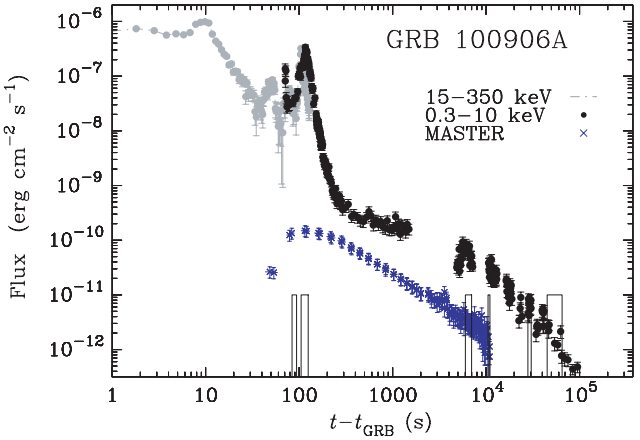

Figure 3. The optical light curve of GRB 100906A obtained by MASTER with one polarization filter (blue dots with 20 per cent error bars resulting from the uncertainty of the magnitude–flux conversion – see Section 3.2; data are corrected for the Galactic extinction) along with the *Swift*/BAT 15–350 keV flux with 1-s binning (grey dots connected by the dot-dashed line; data with negative lower limits are not shown) and the *Swift*/XRT 0.3–10 keV unabsorbed-flux light curve (black dots; Beardmore & Markwardt 2010). Thin-line rectangles show the time intervals selected for spectral analysis.

Two MASTER telescopes, at Tunka and Blagoveschensk, were pointed to the GRB position, 38 s after the BAT trigger time *T*0 and 58 s after *T*0, respectively. Because a pilot instrument was mounted at the time at the Blagoveschensk site,[6] we present only the data obtained by the telescope at Tunka. At Kourovka and Kislovodsk, the weather conditions were not suitable for observations.

A bright optical transient was localized by MASTER at the *Swift*/UVOT position (Markwardt et al. 2010), 13 mag at maximum. During the first hour after the trigger time, 24 images in unfiltered light at two polarization angles were produced by the Tunka telescope. Fig. 3 shows the early observations of GRB 100906A in optical and in the 0.3–10 and 15–150 keV energy ranges (see also Fig. 4 and Table 4). A movie of the optical burst of GRB 100906A, as seen at Tunka, is available on the Internet.[7]

We calculate the relative difference between the signals coming from the two polarization filters, for the time interval 100–10^4 s after *T*0. This is less than the relative measuring accuracy of filters of 2 per cent, which is estimated using the observations of standard stars. Unfortunately, technical limitations do not allow us to draw a decisive conclusion about the polarization degree of GRB 100906A (see Section 5.1 and Appendix A).

[6] Since 2010 December, the Blagoveschensk telescope has been in full operating mode.
[7] http://master.sai.msu.ru/static/GRB/grb100906.avi

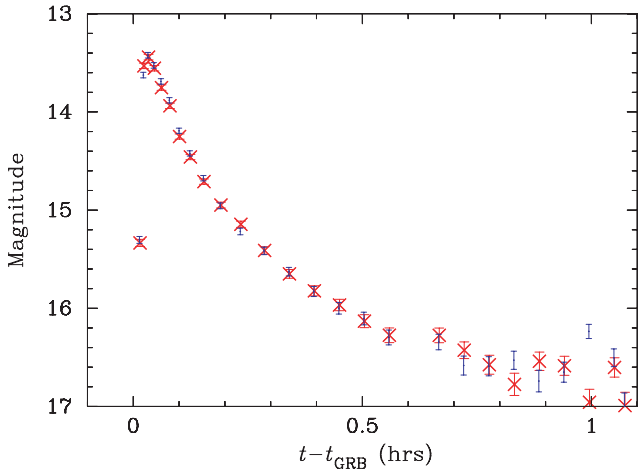

Figure 4. MASTER light curve of GRB 100901A in two polarizations, unfiltered band (blue dots and red crosses). Data are not corrected for the Galactic extinction.

Table 4. Photometry data for GRB 100906A by MASTER in the unfiltered band with two orthogonal polarizing filters. This is a sample of the full table, which is available as Supporting Information with the electronic version of the article.

	$P_{\updownarrow}$			$P_{\leftrightarrow}$	
$t-T0$ (h)	Exp. (s)	Unfiltered (mag)	$t-T0$ (h)	Exp. (s)	Unfiltered (mag)
0.013495	10	15.30 ± 0.04	...	...	...
0.021896	10	13.62 ± 0.03	0.023187	10	13.53 ± 0.03
0.032043	20	13.42 ± 0.03	0.033377	20	13.44 ± 0.03
0.044763	30	13.53 ± 0.03	0.046099	30	13.55 ± 0.03
0.060409	40	13.69 ± 0.03	0.061662	40	13.75 ± 0.03
0.078794	50	13.88 ± 0.03	0.080028	50	13.94 ± 0.03
0.099815	60	14.19 ± 0.03	0.101093	60	14.25 ± 0.03
0.123506	70	14.42 ± 0.03	0.124784	70	14.46 ± 0.03
0.152931	90	14.68 ± 0.03	0.154302	90	14.71 ± 0.03
0.189999	110	14.96 ± 0.03	0.191257	110	14.95 ± 0.03

The 1.5-m OSN telescope observed the GRB a few hours after $T0$ (Fig. 5 and Table 5). The calibration for the *BVIR* bands is carried out using 49 United States Naval Observatory (USNO) stars; the calibration for the U band uses a Landolt star observation. Aperture photometry is carried out using `phot` as implemented in IRAF with a radius equal to the seeing. The error of the afterglow magnitude was obtained by adding quadratically the statistical error given by `phot` and the zero-point error determined with the 49 field reference stars. In addition, Table 6 shows the late photometry obtained by the 2.56-m NOT.

The redshift of the host galaxy $z = 1.727$ was obtained with the Gemini North telescope (Tanvir, Wiersema & Levan 2010).

2.5 Limits on the prompt and afterglow optical flux of GRB 101020A

On 2010 October 10, at 23:40:41 UT, the *Swift*/BAT triggered and located GRB 101020A (Saxton et al. 2010). Sakamoto et al. (2010a) found $T_{90} = 175 \pm 28$ s. The MASTER telescope at Kourovka was pointed to the position of GRB 101020A 106 s after $T0$ at a large zenith distance of 80° (Krushinski et al. 2010b,c). It was observed with two optical tubes. No optical transient is detected with the upper

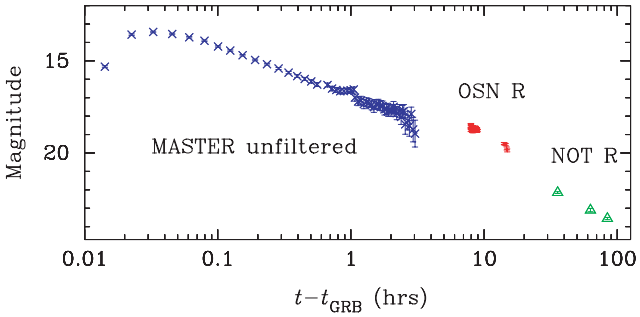

Figure 5. The R-band light curve of GRB 100906A from the OSN and NOT telescopes (red bars and green triangles with small error bars, respectively). For the MASTER unfiltered band, one polarization light curve is plotted by blue crosses before 5 h. Data are not corrected for the Galactic extinction.

Table 5. *UBVRI* photometry for GRB 100906A obtained by the OSN telescope. Reported times are the middle times of exposures. The dots represent 50 observations that are available as Supporting Information with the electronic version of the article.

Band	$t-T0$ (h)	Exposure time (s)	Magnitude
R	7.920835	36	18.53 ± 0.12
R	7.935742	36	18.72 ± 0.12
...	...	...	...
R	8.913334	60	18.77 ± 0.06
R	14.091390	180	19.49 ± 0.06
R	14.217964	180	19.50 ± 0.06
R	14.540464	180	19.55 ± 0.06
R	14.784353	180	19.76 ± 0.08
R	14.928057	180	19.86 ± 0.08
R	38.528342	2×300	> 21.5
V	14.141108	180	19.91 ± 0.20
V	38.402228	300	> 21.0
B	14.193888	300	20.65 ± 0.22
B	38.318343	5×300	> 21.0
I	14.278609	2×180	19.46 ± 0.12
U	14.571669	2×900	> 17.5
U	38.234160	300	> 16.5

limits in the V band, as reported in Table 7, where magnitudes are obtained from co-added images.

3 DATA REDUCTION AND ANALYSIS FOR GRB 100901A AND GRB 100906A

3.1 MASTER astrometric and photometric calibration

Each MASTER telescope is equipped with a set of Johnson/Bessell filters and two linear polarizing laminated films. For every image, astrometric calibration is performed using `imcoords` of IRAF v2.14. Aperture photometry is done using the `phot` package of IRAF (Tody 1993). Standard stars from 13.5 to 17 mag are selected from the Sloan Digital Sky Survey (SDSS) Data Release 7 (DR7; Abazajian et al. 2009). The influence of atmospheric transparency variations on instrumental stellar magnitudes is eliminated following an algorithm described in Everett & Howell (2001). Stars with variations exceeding threefold the errors calculated by IRAF from signal-to-noise information are excluded from the list, and the remaining standard stars are related to SDSS-DR7 data, as suggested

Table 6. *R* magnitudes of GRB 100906A obtained by the NOT.

$t_{start} - T0$ (h)	$t_{end} - T0$ (h)	Exp. time (s)	*R* (mag)
35.031028	36.338862	3×600	22.15 ± 0.05
62.828250	63.078251	900	23.10 ± 0.09
84.046943	84.763888	2×900	23.56 ± 0.06

Table 7. Upper limits on the optical flux in the *V* band for GRB 101020A obtained for co-added images.

$t_{start} - T0$ (s)	t_{middle} (s)	Exp. time (s)	*V* (mag)	Co-added number
106	116	20+20	14.9	1+1
472	2836	4300	18.5	25

by Lupton (2005):[8]

$$B = g + 0.1884\,(u - g) + 0.1313,$$

$$V = g - 0.5784\,(g - r) - 0.0038,$$

$$R = r - 0.2936\,(r - i) - 0.1439,$$

$$I = i - 0.3780\,(i - z) - 0.3974. \quad (1)$$

Here, *BVRI* are the Johnson system and i, r, g and z are the Sloan Survey photometric system (all in the Vega system). The resulting lists of standard stars are given in Tables 8 and 9 for GRB 100901A and GRB 100906A, respectively. Associated variances between observed and catalogue values after applying the above relations in different filters are 0.005–0.008 mag. In our observations, the standard deviations of light curves of the standard stars are greater, 0.02–0.1 mag, depending on the filter. For images obtained in the unfiltered band, we use a zero-point correction to the unfiltered magnitudes obtained at the Kislovodsk MASTER telescope. Flux calibration of the unfiltered magnitudes at Kislovodsk is described in Section 3.2.

The GRB magnitude errors are defined by the standard deviation of the brightness variations of the standard stars of similar magnitude in the case of a high signal-to-noise ratio. For a low signal-to-noise ratio, we lack standard stars of such magnitudes. To estimate observational errors, we take the theoretical limit for errors following the basic CCD equation. This limit is much greater (up to 2 mag at >18 mag) than the expected amplitude variations of standard stars at such a signal-to-noise level.

For each of the standard stars, we evaluate the difference between its average magnitudes in both orthogonal polarizations. Assuming that the light of standard stars should not be polarized, standard stars with outlier polarization are excluded from the list. Afterwards, corrections are applied to match the average magnitudes of the standard stars in two polarizations. The relative accuracy of observations with two filters is approximately 2 per cent, based on observations of standard stars.

[8] http://www.sdss.org/dr7/algorithms/sdssUBVRITransform.html

3.2 MASTER flux calibration

To convert magnitudes *BVRI* into absolute values, we use the zero-magnitude flux densities of the Landolt photometry (see, for example, Pickles & Depagne 2010). To convert CCD photometry into absolute fluxes without a colour filter interposed (i.e. in a wide waveband; see Fig. 6), we use the Pogson formula relating stellar magnitudes and CCD band-integrated flux with a zero-magnitude flux, calculated using the Vega spectrum given by Hayes (1985).

The standard stars are designated with the *W* and *P* magnitudes: obtained from observations in the wide waveband and in the wide waveband plus polarizer. Both are approximated by the formula $0.8\,R + 0.2\,B$. This formula is arrived at by a compilation of colour diagrams $W - X$ versus $B - R$, where X is a combination of stellar magnitudes, $X = a\,R + b\,B$. In a general case, points group around a straight oblique line. The zero slope of the relation is achieved by fitting for the parameters a and b. It is found that, for the white light, the above representation of the wide-band magnitudes holds with an accuracy of 4 per cent for *W* magnitudes and 2 per cent for *P* magnitudes. Unfortunately, for the polarizer that we used in the observations, there was a long-wavelength interval with an unspecified transmission efficiency function. Simulating the polarizer transmission function in different ways and folding it with different spectra (Vega, $\propto \nu^{-1}$ and $\propto \nu^{0}$), we have estimated the maximum additional uncertainty of ∼20 per cent. Thus, we add 20 per cent of uncertainty when we convert *P* to absolute fluxes.

The observed magnitude *W* of an investigated source is converted into the absolute flux value using the Pogson equation

$$F^W_{GRB} = F^W_o \times 10^{-0.4\,W}. \quad (2)$$

Here, F^W_o is the calculated Vega flux in the CCD spectral band:

$$F^W_o = \int F_{Vega}(\lambda)\,W(\lambda)\,d\lambda = 1.33 \times 10^{-5}\ \mathrm{erg\,cm^{-2}\,s^{-1}}. \quad (3)$$

In the same way, magnitudes *P* are converted to flux values using equation (2) with the zero-magnitude flux

$$F^P_o = \int F_{Vega}(\lambda)\,P(\lambda)\,d\lambda = 1.16 \times 10^{-5}\ \mathrm{erg\,cm^{-2}\,s^{-1}}. \quad (4)$$

In the above expressions, $W(\lambda)$ and $P(\lambda)$ are, respectively, the normalized CCD response function and its normalized convolution with the transmission efficiency of the polarizer (see the right panel of Fig. 6). Of course, if a source is observed with partly (linearly) polarized light through such a polarization filter, full information on the degree of polarization and its angle is needed in order to derive the total flux. For an unpolarized source, or for a source with equal signals from two polarizers (as in the case of GRB 100906A), we can safely use equation (4). For details, we refer to Appendix A.

To obtain the GRB's flux density at the wavelength of the CCD response maximum, 5500 Å, we divide flux F^W_{GRB} or F^P_{GRB} by an effective frequency interval $\Delta\nu_{eff}$ of the corresponding response function. Naturally, the value of $\Delta\nu_{eff}$ depends on a particular spectral distribution. The effective frequency interval of the CCD response function is $\sim 3.9 \times 10^{14}$ Hz, calculated as the mean of values $\Delta\nu_{eff}$ for the Vega spectrum, white light and power-law spectrum with -1 slope, all falling inside a 15 per cent uncertainty interval. The effective frequency interval of the CCD plus polarizer, calculated in the same way, is $\sim 3.2 \times 10^{14}$ Hz with a 10 per cent uncertainty interval. Bearing in mind that a real spectrum might be something different from the three considered in such a simple analysis, we assume approximately a 20 per cent accuracy for converting from flux units to spectral flux density units.

Table 8. Stars from the SDSS-DR7 used as standard stars for GRB 100901A. Columns 3–7 contain SDSS *ugriz* magnitudes (Vega system). Column 8 contains the average unfiltered *W*-band MASTER magnitude. This is a sample of the full table, which is available as Supporting Information with the electronic version of the article.

Source ID	SDSS name	*u* (mag)	*g* (mag)	*r* (mag)	*i* (mag)	*z* (mag)	*W* (mag)	RA (J2000) (d)	Dec. (J2000) (d)
1	J014906.68+224024.7	19.246	17.05	15.96	15.462	15.161	15.95	27.277834	22.673535
2	J014904.39+224045.3	15.841	14.609	14.143	13.953	13.897	14.21	27.26829	22.679256

Table 9. Standard stars used for the photometry of GRB 100906A. Column 3 contains the average unfiltered *P*-band MASTER magnitude measured with one of the polarization filters. This is a sample of the full table, which is available as Supporting Information with the electronic version of the article.

Source ID	USNO-A2.0 name	$P_{\updownarrow}$ (mag)	Standard deviation of light curve (mag)	$\langle P_{\updownarrow}\rangle - \langle P_{\leftrightarrow}\rangle$ (mag)	RA (J2000) (d)	Dec. (J2000) (d)
(1)	(GRB 100906A)	...	1.14	0.01	28.68413	55.63050
2	1425–02624804	15.70	0.04	−0.04	28.69122	55.63834

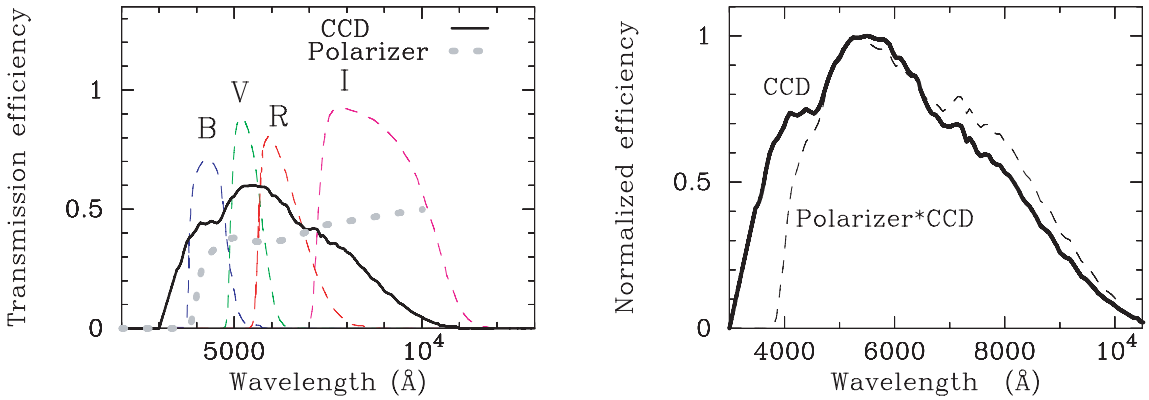

Figure 6. In the left panel, the MASTER filter transmission efficiencies are plotted along with those of the CCD and polarizer. In the right panel, functions $W(\lambda)$ and $P(\lambda)$ are shown, which are the bandpasses of the CCD and of the CCD plus polarizer, respectively.

3.3 *Swift* BAT and XRT light curves

In order to build flux light curves observed by *Swift*/BAT (Figs 1 and 3), standard sets of GRB products are obtained using the ftool `batgrbproduct` within HEASOFT v6.10, and the count light curves in 15–350 keV are retrieved. The 15–150 keV spectra averaged over the total fluence time interval are analysed in XSPEC (Arnaud 1996) using the power-law approximation. The derived spectral parameters are used to calculate the 15–350 keV model flux and to obtain counts to flux conversion factors in the 15–350 keV range. Thus, we apply constant conversion factors 1.07×10^{-6} and 9.17×10^{-7} erg cm^{-2} counts^{-1} for GRB 100901A and GRB 100906A, respectively.

The *Swift*/XRT 0.3–10 keV unabsorbed light curves are available from the *Swift* Burst Analyser. These light curves are produced with information on the spectral evolution involved (Evans et al. 2010). The late-time spectra of GRBs, available from the *Swift* Spectra Repository, are the source for the estimates of the column densities for the soft X-ray absorption.

3.4 Spectral fitting

In order to build simultaneous wide-energy spectra, we select time intervals that are covered by the optical observations. The prompt stage of GRB 100901A (before T_{90}) contains three suitable MASTER exposure intervals: $t - T0 = 193$–233, 312–372 and 387–467 s, where $T0$ is the trigger time. There are two MASTER time intervals during the prompt stage of GRB 100906A overlapping with the observations by *Swift*/XRT, 73.8–83.8 s and 105–125 s (or very close, in the first case).

We download the X-ray time-sliced spectra, constructed for the time intervals of the optical exposures, from the *Swift* Spectra Repository (Evans et al. 2009). For GRB 100906A, we also use the results obtained by the Konus–*Wind* (Golenetskii et al. 2010). The BAT spectra and response matrices are prepared as described in the Data Analysis Guidelines.[9] These are extracted for the selected time intervals and corrected using the tasks `batbinevt`, `batupdatephakw` and `batphasyserr`, and a response matrix generated by the `batdrmgen` task. Then, the spectra are fitted in XSPEC v12.6 using models `powerlaw` (power law), `cutoffpl` (cut-off power law) or `grbm` (Band function), in combination with absorption components. When simultaneous fits for the 0.3–10 and 15–150 keV and/or optical data are performed, the XRT spectra are rebinned using `grppha`, to ensure that there are at least 20 counts per bin, which is necessary for joint minimization of χ^2.

[9] http://swift.gsfc.nasa.gov/docs/swift/analysis/threads/batgrbproductthread.html

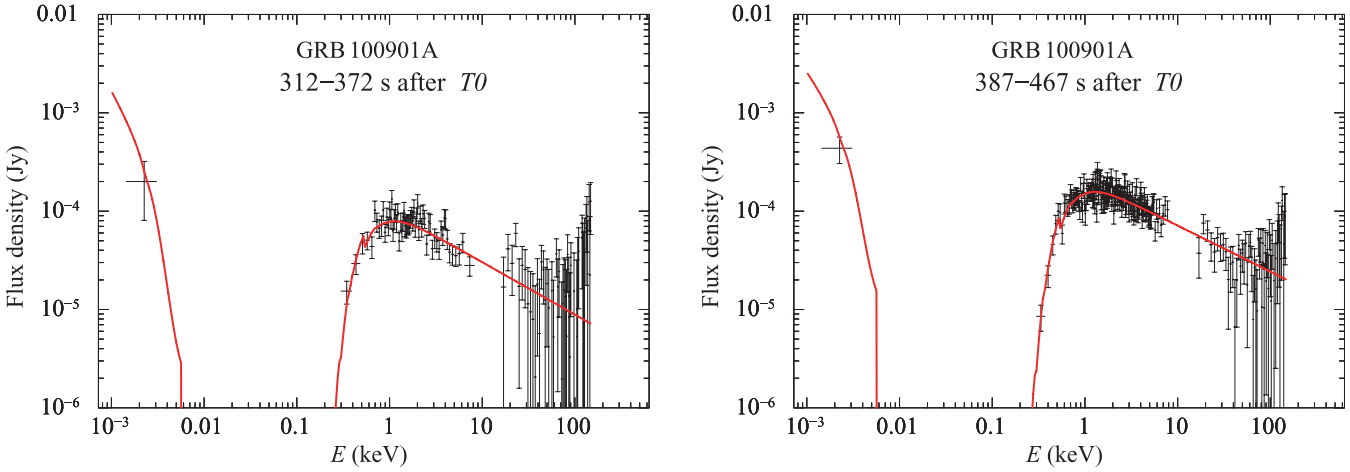

Figure 7. Spectrum of GRB 100901A for two time intervals at $t \lesssim T_{90}$. The optical flux density obtained by MASTER and corrected for the Galactic extinction $A_V = 0.327$ (NED; Schlegel et al. 1998), is shown by the single left point, whose horizontal bar corresponds to the MASTER unfiltered effective frequency interval. Spectra in 0.3–10 and 15–150 keV are made with the *Swift* BAT and XRT data. Best-fitting absorbed power laws are shown by the red lines. Their spectral parameters are described in Table 10 as Fit 100901.2 for 312–372 s and Fit 100901.3 for 387–467 s).

To account for the soft X-ray absorption, we use the XSPEC model components `phabs` (Galactic absorption) and `zphabs` (absorption in the host galaxy). When we fit the parameters of the optical extinction in the GRB host, we use the XSPEC model `zdust`, which is the extinction by the dust grains. In the fits, whose results are presented in Tables 10, 12 and 13 in the next section, we assume a Small Magellanic Cloud (SMC) type for the host galaxy extinction curve and the total-to-selective extinction $R_V = 2.93$ (Pei 1992), following the results of the studies by Jensen et al. (2001) and Schady et al. (2010). We discuss variations resulting from the different extinction laws in the text. Correction for the reddening in the Galaxy is done beforehand, using the values calculated using the NASA/IPAC Extragalactic Database (NED) Galactic Extinction calculator,[10] based on the work of Schlegel, Finkbeiner & Davis (1998).

To analyse the late-time spectra, we consider the optical observations after 10 T_{90}. First, we check that large variations of X-ray flux are absent in a time interval – we request that the flux density at 10 keV varies by less than a factor of 3. The X-ray data are rebinned to a minimum of 10 (20, if possible) counts per bin (using `grppha`). The optical data are averaged over the time interval and transformed by the task `flx2xsp`. We check that the number of degrees of freedom in the fit by the XSPEC model `phabs*zphabs*zdust*powerlaw` is more than 5. The selected time intervals are depicted by rectangles in Figs 1, 3 and 11.

4 RESULTS

4.1 Spectra of GRB 100901A and GRB 100906A before T_{90}

For the three early spectra of GRB 100901A (Fig. 7), fits with an absorbed power law are satisfactory (Fits 100901.1, 100901.2 and 100901.3 in Table 10). Other spectral models, a cut-off power law and the Band function do not improve the fitting statistics.

For GRB 100906A, we do not include the host-galaxy absorption model component, as its spectral distributions from optical to X-ray (Fig. 8) cannot apparently be fitted by a single power law. Generally, for a variable complex spectrum of an early GRB emission, it is impossible to estimate the extinction in the optical band, as it is not possible to use a priori information about the spectral distribution. Table 11 contains the parameters of the fits by the Band model, together with the resulting values of χ^2 for the alternative models with fewer free parameters, which give worse results. We also calculate the slopes of the photon spectrum between the MASTER points and the best-fitting 3-keV flux densities (column 3 in Table 11). We note that the optical points are corrected for the Galactic extinction.

Apparently, the peak of the spectral energy distribution (SED) of GRB 100906A is located somewhere around 0.3–30 keV at times 80–120 s, and moves gradually to soft energies. The SED peak energy $E_{\rm peak}$ for the Band spectrum is $(-\alpha_{\rm B} + 2) \times E_0$, where $\alpha_{\rm B}$ is the photon index of the lower-energy part of the Band function and E_0 is the characteristic energy for the Band function (Table 11). We find that $E_{\rm peak}$ shifts from about 30 to 4 keV between the two spectral distributions presented in Fig. 8. The higher-energy part of the spectrum of GRB 100906A (>30 keV) can be fitted by a single power law. This is consistent with the Konus–*Wind* results (Fig. 8, dotted line). According to Golenetskii et al. (2010), the spectrum of the second bursting episode of GRB 100906A, observed by Konus–*Wind* in γ-rays from 98.304 to 122.880 s, is best fitted in the 20 keV–2 MeV range by a power-law model with the photon index $2.55^{+0.25}_{-0.2}$.

4.2 Host galaxy extinction of GRB 100901A

We fit several late-time spectra comprising *Swift*/XRT data and simultaneous optical points available from MASTER. The optical points are the time-averaged unfiltered W magnitudes as follows: 18.05 ± 0.03, 17.78 ± 0.02, 17.61 ± 0.04 and 19.30 ± 0.02 mag, corrected for the Galactic extinction $A_V = 0.327$ (NED; Schlegel et al. 1998), successively for the fits in Table 12. Just as for the prompt spectra, we can approximate the late-time spectra of GRB 100901A by an absorbed power-law model.

By averaging the results of the late-time fits (Table 12), we obtain $A_V^{\rm int} = 0.4 \pm 0.2$ and $N_{\rm H}^{\rm int} = (2.2 \pm 0.7) \times 10^{21}$ cm^{-2}. By averaging the results of the three early fits (Table 10), we obtain $A_V^{\rm int} = 0.8 \pm 0.1$ and $N_{\rm H}^{\rm int} = (5.1 \pm 0.6) \times 10^{21}$ cm^{-2}. There is an apparent change in the values of $N_{\rm H}^{\rm int}$ and $A_V^{\rm int}$ between the prompt-time and late-time fit parameters. It is likely that the prompt-time value of $N_{\rm H}^{\rm int}$

[10] http://ned.ipac.caltech.edu/forms/calculator.html

Table 10. Spectral parameters for GRB 100901A at the prompt stage resulting from the simultaneous fitting of the absorbed power law in XSPEC (`phabs*zphabs*zdust*powerlaw`) to the MASTER, XRT and BAT data (Fig. 7). The Galactic absorption column density is fixed at $N_{\rm H} = 7.1 \times 10^{20}$ cm^{-2} (Kalberla et al. 2005). The assumed host galaxy extinction curve is SMC type and the total-to-selective extinction is $R_V = 2.93$. Columns 4 and 5 give the fitted intrinsic absorption column density and optical extinction at $z = 1.408$, respectively.

Fit ID	$t - T0$ (s)	Photon index	$N_{\rm H}^{\rm int}$ (10^{22} cm^{-2})	$A_V^{\rm int}$	χ^2/dof
100901.1	193–233	1.60 ± 0.08	0.6 ± 0.2	$1.1^{+0.6}_{-0.3}$	73.4/94
100901.2	312–372	1.53 ± 0.05	0.4 ± 0.1	$0.95^{+0.4}_{-0.2}$	138/134
100901.3	387–467	1.49 ± 0.02	0.55 ± 0.07	$0.75_{\pm}0.1$	216/219

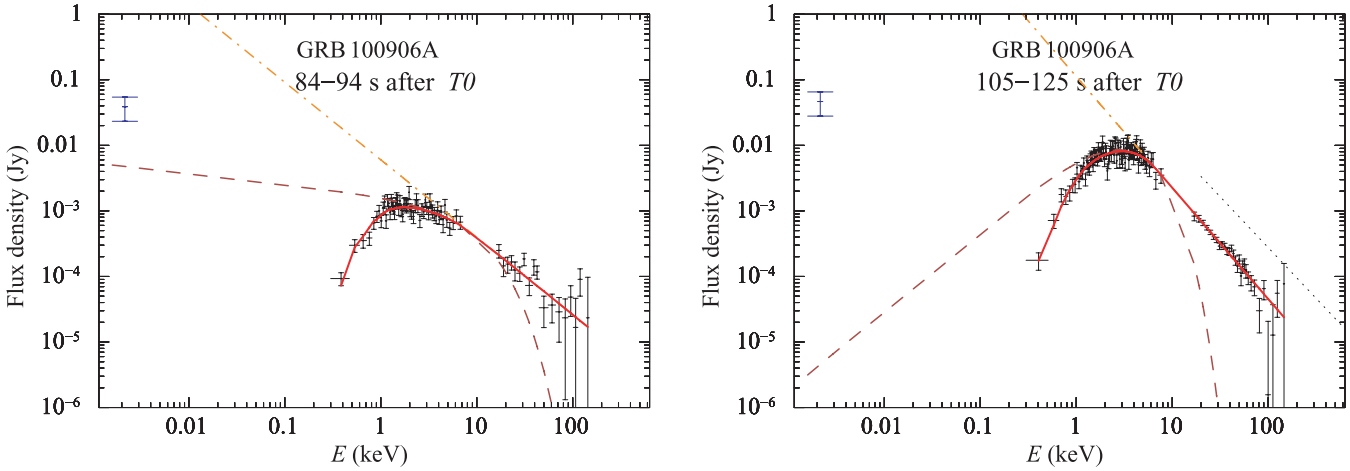

Figure 8. Spectrum of GRB 100906A for two time intervals at $t \lesssim T_{90}$. Optical points are corrected for the Galactic extinction $A_V = 1.194$ (NED; Schlegel et al. 1998). In the left panel, we use the MASTER observation at 73.8–83.8 s. Best-fitting absorbed Band functions are shown by the red lines (Fits 100906.1 and 100906.2 in Table 10). The brown dashed line depicts the unabsorbed low-energy part, and the orange dot-dashed line shows the unabsorbed high-energy part. The dotted power law represents observations of Konus–*Wind* from 98.304 to 122.880 s for 20 keV–2 MeV with a correct slope and a roughly estimated flux. No attempt has been made to estimate the optical extinction in the GRB host galaxy.

Table 11. Spectral parameters for GRB 100906A at the prompt stage resulting from the fitting of the absorbed Band function in XSPEC (`phabs*zphabs*grbm`) to the XRT and BAT data (Fig. 8). The Galactic absorption column density is fixed at $N_{\rm H} = 2.2 \times 10^{21}$ cm^{-2} (Kalberla et al. 2005). Column 3 gives the photon index between the optical and modelled 3-keV flux density, and columns 4–7 show the photon indices and characteristic energy of the Band function and the intrinsic absorption at $z = 1.727$, respectively. In the last three columns, χ^2 statistics of the fits shown in Fig. 8 are given in bold, with the statistics of fits with alternative models in normal font.

Fit ID	$t - T0$ (s)	MASTER–XRT 2.2 eV–3 keV	Photon indices of Band function		E_0 (keV)	$N_{\rm H}^{\rm int}$ (10^{22} cm^{-2})	χ^2/dof Band	χ^2/dof power law	χ^2/dof cut-off pow
100906.1	84–94[a]	1.50 ± 0.06	1.2 ± 0.2	$2.18^{+0.08}_{-0.07}$	9^{+7}_{-4}	$0.1^{+0.3}_{-0.1}$	**112/110**	141/112	121/111
100906.2	105–125	1.24 ± 0.06	$-0.22^{+0.24}_{-0.07}$	2.70 ± 0.03	$2.3^{+0.4}_{-0.1}$	$0^{+0.23}_{-0.0}$	**149/139**	314/141	254/140

[a] The MASTER observation was carried out in a slightly earlier time interval, 73.8–83.8 s.

Table 12. Spectral parameters for GRB 100901A at late time intervals. An XSPEC fitting of the absorbed power law to the MASTER and XRT/*Swift* data is performed. Frozen fit parameters are the same as for the fits in Table 10.

Fit ID	$t - T0$ (s)	Photon index	$N_{\rm H}^{\rm int}$ (10^{22} cm^{-2})	$A_V^{\rm int}$	χ^2/dof
100901.4	5000–6500	2.1 ± 0.1	0.3 ± 0.1	$0.8^{+0.5}_{-0.4}$	15.8/14
100901.5	15 000–17 500	2.0 ± 0.1	$0.1^{+0.2}_{-0.1}$	$0.2^{+0.3}_{-0.2}$	38.6/38
100901.6	27 000–28 500	2.1 ± 0.1	0.3 ± 0.2	$0.4^{+0.4}_{-0.3}$	36.6/35
100901.7	102 800–121 500	$2.10^{+0.01}_{-0.11}$	0.28 ± 0.25	$0.5^{+0.8}_{-0.2}$	13.0/10

is biased because of the spectral evolution, and probably because the prompt spectral shape is not precisely power-law in the range from optical to X-ray. Butler & Kocevski (2007) and Evans et al. (2010) argue that absorption derived from early-time XRT data, when a strong spectral evolution is present, can be misleading.

The late-time spectrum compiled at the *Swift*/XRT Spectrum Repository (UK *Swift* Science Data Centre) for 4000–33 229 s yields the value of the intrinsic $N_{\rm H}^{\rm int} = (2.9 \pm 0.9) \times 10^{21}$ cm^{-2} (90 per cent uncertainty interval), which is in very good agreement with our fit results for the late-time sliced spectra. This indicates that a power-law approximation for the X-ray spectrum of GRB 100901a is a good approximation for any late-time interval.

We have also tried other types of extinction laws in the GRB host. In addition to the fits presented in Table 12, we performed fits with different extinction laws in the host galaxy: that of the LMC (Large Magellanic Cloud) and MW (Milky Way). For these, we applied different values of R_V (Pei 1992, see below). The quality of the fits and the values of $N_{\rm H}$ remain the same, because the choice of optical extinction does not greatly affect the amount of soft X-ray absorption. We have found that, depending on the extinction law applied, for three late-time intervals, the average total extinction $A_V^{\rm int} = R_V\, E(B-V)^{\rm int}$ varies as $\langle A_V^{\rm int}\rangle = 0.4 \pm 0.2$ (SMC, $R_V = 2.93$), $\langle A_V^{\rm int}\rangle = 0.5 \pm 0.2$ (LMC, $R_V = 3.16$) and $\langle A_V^{\rm int}\rangle = 0.7 \pm 0.2$ (MW, $R_V = 3.08$).

Based on the 'late-time' values of the optical extinction in the GRB host, we calculate the ratio $N_{\rm H}^{\rm int}/A_V^{\rm int}$, which equals $(5 \pm 2) \times 10^{21}$ cm^{-2} (for the SMC type of extinction in the GRB host), $(4 \pm 2) \times 10^{21}$ cm^{-2} (LMC) and $(3 \pm 1) \times 10^{21}$ cm^{-2} (MW). These are not far from the ratios empirically found for the SMC, LMC and MW: $\sim 4 \times 10^{21}$ cm^{-2} (SMC), $\sim 3.5 \times 10^{21}$ cm^{-2} (LMC) and $\sim 2 \times 10^{21}$ cm^{-2} (MW; e.g. Schady et al. 2010). Thus, independent of the extinction law used, the resulting metal-to-dust ratio in the host of GRB 100901A is comparable to the level measured for the MW, SMC or LMC.

4.3 Host galaxy extinction of GRB 100906A

Three late-time spectral distributions are shown in Figs 9 and 10. The parameters of the fits are listed in Table 13. The optical points are the time-averaged unfiltered P magnitudes by MASTER (17.54 ± 0.05 for 6000–7000 s and 18.7 ± 0.3 for 10 500–11 000 s) and OSN ($R = 18.70 \pm 0.02$ for 28 000–30 400 s). The optical point in the R band at 50 000–54 000 s is obtained by averaging the OSN data ($R = 19.7 \pm 0.3$) and the V, B and I points can be found in Table 5. Before the fitting, the optical data are corrected for the Galactic extinction calculated in the NED Extragalactic Calculator: $A_V = 1.194$, $A_B = 1.554$, $A_R = 0.963$ and $A_I = 0.699$ (NED; Schlegel et al. 1998).

We can see that the optical data at $\sim$14 h (Fig. 10) are best fitted by an absorbed broken power law with a peak in the optical range. However, we cannot consider this peak robust because the optical points are non-simultaneous, and there is a strong variation observed in the R band around 14 h (see Fig. 5).

The parameters of the Fit 100906.3 (the first three lines in Table 13) are obtained by simultaneously fitting the spectral data at the three time intervals. The spectral slopes and normalization parameters vary between the spectra, while $E(B-V)^{\rm int}$ (i.e. $A_V^{\rm int}$) and $N_{\rm H}^{\rm int}$ are forbidden to change. This was done in an attempt to increase statistics to obtain a positive 1σ interval for $A_V^{\rm int}$. Nevertheless, we can report only the 2σ upper limit. Setting other types of extinction law in the host galaxy does not change the value of $A_V^{\rm int}$.

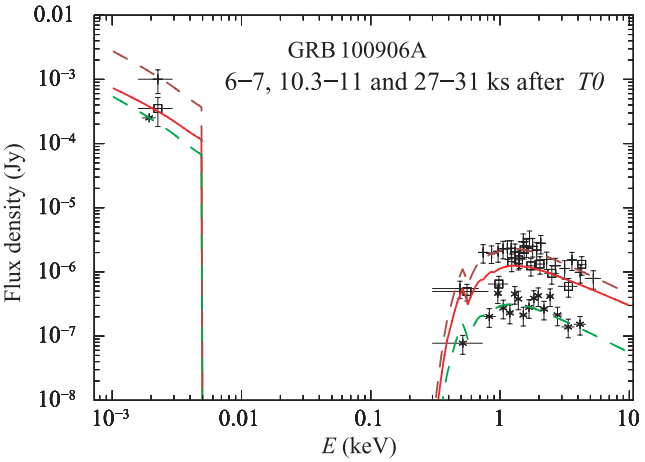

Figure 9. Spectral distributions of GRB 100906A at three time intervals: 6000–7000, 10 500–11 000 and 28 000–30 400 s (points, squares and crosses with bars, respectively). The optical data are as follows: MASTER, $P = 17.54 \pm 0.05$ for 6000–7000 s, $P = 18.7 \pm 0.3$ for 10 500–11 000 s; OSN, $R = 18.70 \pm 0.02$ for 28 000–30 400 s, additionally corrected for the Galactic extinction $A_V = 1.194$ and $A_R = 0.963$ (NED; Schlegel et al. 1998). Lines show the best-fitting absorbed power laws, whose parameters are listed as Fit 100906.3 in Table 13.

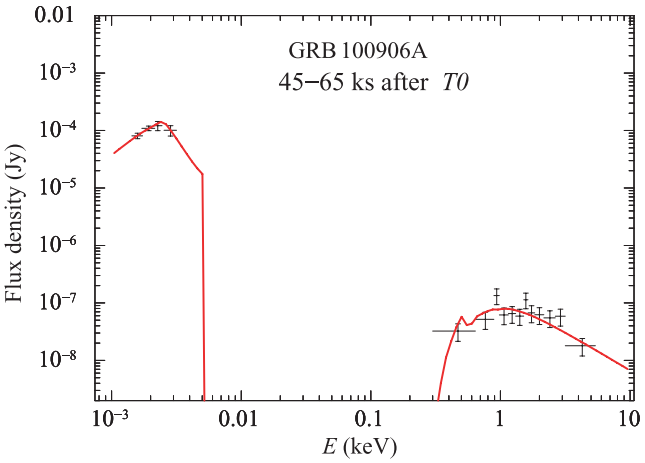

Figure 10. Spectrum of GRB 100906A compiled from the XRT data in the interval 45–65 ks and optical *BVIR* observations obtained by the OSN around 14 h after the trigger (in the interval 50.9–54.0 ks) and corrected for the Galactic extinction. The solid line is the best-fitting absorbed broken power-law model, whose parameters are listed as Fit 100906.4 in Table 13.

The spectrum of GRB 100906A at the 10–50 ks interval from the *Swift*/XRT Spectrum Repository (at the UK *Swift* Science Data Centre) yields the value of intrinsic $N_{\rm H}^{\rm int} = (8.5 \pm 3) \times 10^{21}$ cm^{-2} (with a 90 per cent uncertainty interval). The values of $N_{\rm H}^{\rm int}$ in Table 13 with 1σ errors are consistent with this value. If we take the lower 2σ limit of the XRT repository value, $N_{\rm H}^{\rm int} = 4.8 \times 10^{21}$ cm^{-2}, and the upper 2σ limit on $A_V^{\rm int}$ obtained for different extinction laws, we arrive at the lower 2σ limit on $N_{\rm H}^{\rm int}/A_V^{\rm int} \approx 1.1 \times 10^{22}$. This limit is at least twice the typical ratio, empirically defined for the MW, SMC and LMC (see Section 4.3). This ratio is consistent with the results of Schady et al. (2010). They studied 28 GRBs and found values of $N_{\rm H}^{\rm int}/A_V^{\rm int}$ typically higher than those for the MW, SMC and LMC.

Table 13. Spectral parameters for GRB 100906A at several late time intervals (Figs 9 and 10). An XSPEC fitting of the absorbed power law or broken power law to the MASTER, OSN and XRT/*Swift* data is performed. The Galactic absorption column density is $N_{\rm H} = 2.21 \times 10^{21}$ cm^{-2} (Kalberla et al. 2005). The host galaxy extinction curve is that of the SMC and the total-to-selective extinction is taken to be $R_V = 2.93$. The column designation is the same as for Table 12 with the addition of a lower photon index (left) and the break energy in eV.

Fit ID	$t - T0$ (s)	Photon index	$E_{\rm break}$ (eV)	Photon index	$N_{\rm H}^{\rm int}$ (10^{22} cm^{-2})	$A_V^{\rm int}$	χ^2/dof
100906.3	6000–7000	...	...	1.96 ± 0.05	$0.4^{+0.3}_{-0.2}$	< 0.4	36.6/42
	10 500–11 000	...	...	1.9 ± 0.1			
	28 000–30 400	...	...	2.01 ± 0.02			
100906.4	45 000–65 000	-1.3 ± 0.7	2.5 ± 0.3	2.34 ± 0.04	$0.25^{+0.55}_{-0.25}$	0.35 ± 0.09	9.78/10

We conclude that, for GRB 100906A, our fitting provides only the upper limit on $A_V^{\rm int}$. There are indications that this GRB has a high $N_{\rm H}^{\rm int}/A_V^{\rm int}$ ratio, which could be the result of a dust destruction resulting from γ-radiation or the intrinsic properties of the host galaxy.

4.4 Jet break time of GRB 100906A

We construct broken power-law fits to the light curves of GRB 100906A after 10 ks. Table 14 presents the parameters of the fits. A break on the X-ray light curve is found around ∼50 ks. The parameters of the 0.3–10 keV light curve can be reconciled with the 'closure relations' between the temporal and spectral indices (α and β in $F_\nu \propto t^{-\alpha}\nu^{-\beta}$) in the framework of the fireball model in the following way (see table 1 in Racusin et al. (2009), and references therein and see the reviews of Mészáros 2002; Zhang & Mészáros 2004; Piran 2005). Before the break, for the ISM environment and the 'slow cooling' regime and using $\beta_{\rm XRT} = 1.0 \pm 0.3$, we obtain $\alpha = 3$ and $\beta/2 = 1.5 \pm 0.45$ (cf. $\alpha = 1.68 \pm 0.02$ in Table 14, the first row, before the break). The electron spectral index is $p = 2$ and $\beta + 1 = 3.0 \pm 0.6$. After the break, applying a uniform spreading jet scenario, we arrive at $\alpha = 2$ and $\beta + 1 = 3.2 \pm 0.4$. The electron spectral index has the same functional form $\beta = (p - 1)/2$. The value of β is almost the same ($\beta_{\rm XRT} = 1.1 \pm 0.2$), and we arrive at $p = 3.2 \pm 0.4$. Thus, the closure relations can be satisfied for a consistent value of p. The relations applied imply that $\nu_{\rm m} < \nu_{\rm x} < \nu_{\rm c}$, where $\nu_{\rm m}$ and $\nu_{\rm c}$ are the characteristic synchrotron and cooling frequencies, respectively.

We have tried to find out whether this break is achromatic. The OSN data *R* show that, around 52 ks, there is an abruptness of the *R* light curve (the fit parameters in row 2 of Table 14). However, the time sampling of the OSN *R* data alone is not good enough to clear up the behaviour around this time. If we combine the OSN and NOT data (the third row in Table 14), we apparently do not obtain an achromatic peak, because the tentative break on the *R* light curve shifts to about 35 ks.

The slope of the *R* light curve (OSN + NOT) before the break is obtained by the data, crowded around 30 ks, and might be misleading. If we suggest that the slope of the *R* light curve before the break equals the slope of the MASTER light curve for the earlier data, shown by blue crosses in Fig. 11 (i.e. 1.08; also reported by Kuvshinov et al. 2010), the break time shifts to $39.0^{+0.5}_{-1}$ ks (the temporal slope after the break remains the same, ∼2.2, as in the third row of Table 14).

We conclude that the X-ray data alone indicate a jet break that can satisfy the closure relations. The optical data do not yield confidence about the achromatic characteristic of the break. For a discussion of the Amati and Ghirlanda relations, see Section 5.4.

5 DISCUSSION

5.1 Optical emission sites of GRB 100901A and GRB 100906A

The prompt behaviours of the two closely studied GRBs are quite distinct. For GRB 100901A, we see a similarity of light curves in the optical, γ and X-ray at around 300–500 s after the trigger. For GRB 100906A, there is no such similarity of temporal behaviour. It has a perfectly smooth optical light curve, gradually rising and decaying, which is a different profile from that in the 15–150 keV band (Fig. 3).

From this point of view, GRB 100901A and GRB 100906A support the earlier noticed diversification for optical emission, detected during the first few minutes after the onset of a GRB (e.g. Vestrand et al. 2005, 2006). In some cases, the prompt optical flux variations are correlated with the prompt γ emission, and in other cases early optical afterglow light curve is uncorrelated with the γ-ray light curve.

Such a division of GRBs can be understood within the picture of optical emission generated from different sites of the relativistic jet: in the internal, external forward or reverse shock waves (e.g. Mészáros & Rees 1999; Sari & Piran 1999). The external forward

Table 14. Parameters of the time fits to the GRB 100906A light curves, where slope α is quoted in $F_\nu \propto t^{-\alpha}\nu^{-\beta}$. The first three fits are performed with broken power laws, and the last with the power law. Also given are the spectral indices in the XRT spectral range $\langle\beta_{\rm XRT}\rangle$, retrieved from the *Swift* Burst Analyser and averaged over the relevant time intervals. The time intervals are the two parts of the whole time-span (column 2), divided at the break time (column 5).

Light curve	Time (ks)	Before break		$t_{\rm break}$ (ks)	After break		χ^2/dof
		α	$\langle\beta_{\rm XRT}\rangle$		α	$\langle\beta_{\rm XRT}\rangle$	
3–10 keV	10–300	1.68 ± 0.02	1.0 ± 0.3	51^{+4}_{-3}	$2.9^{+0.1}_{-0.3}$	1.1 ± 0.2	145/78
R (OSN)	28–54	1.36 ± 0.05	1.1 ± 0.2	$51.9^{+0.5}_{-0.2}$	10^{+13}_{-3}	...	56.0/55
R (OSN+NOT)	28 − 310	0.14 ± 0.02	1.1 ± 0.2	$34.9^{+0.5}_{-0.2}$	$2.17^{+0.03}_{-0.04}$	1.0 ± 0.2	135/58
1-3 eV (MASTER)	0.18 − 2.52	1.08 ± 0.02	1.3 ± 0.4	...	...	...	13.9/12

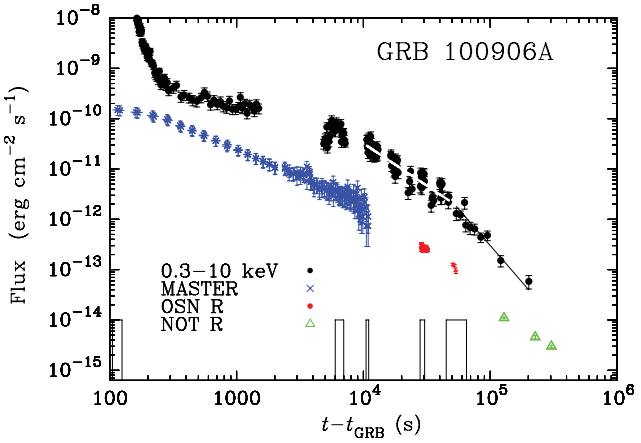

Figure 11. GRB 100906A light curves: unabsorbed 0.3–10 keV flux (black dots) observed by *Swift*/XRT, unfiltered MASTER band flux (blue crosses), *R*-band flux by the OSN (red dots) and *R*-band flux by the NOT (green triangles). The optical points are corrected for the Galactic extinction. The broken power-law fit is plotted over the 0.3–10 keV light curve in white and black, before and after the break time at 51 ks, respectively. Thin-line rectangles show the time intervals selected for spectral analysis.

shocks arise because of the interaction of the ejected material with the ISM and they propagate into the ambient media. The reverse shock propagates into the ejecta itself. The internal shocks are produced because of the collisions among many engine-ejected shells (e.g. Mészáros & Rees 1997; Sari & Piran 1997). The correlation between optical, γ and X-ray can be achieved, if the optical emission is produced by the synchrotron mechanism within the same region as the hard radiation.

The early X-ray and soft γ-ray spectrum of GRB 100901A shows a dependence close to $\nu^{-1/2}$, which is typical for the synchrotron radiation if $\nu_{\rm c} < \nu < \nu_{\rm m}$ (where $\nu_{\rm m}$ and $\nu_{\rm c}$ are the characteristic synchrotron and cooling frequencies, respectively) in the regime when electrons lose energy very quickly (see, for example, Sari, Piran & Narayan 1998; Sari & Piran 1999). Adding the MASTER optical point (corrected for the Galaxy extinction), and fitting simultaneously the optical, 0.3–10 keV and 15–150 keV data by an absorbed power law, we can determine the magnitude of the optical extinction in the host. Consistent values of $A_V^{\rm int}$ and $N_{\rm H}^{\rm int}$ are obtained for the prompt spectral distributions (Table 10), indicating a persisting relation between the optical and high-energy part of the spectrum. Basically, this means that the optical emission is low-energetic photons from the same region that generates the high-energy photons.

We should add that the data can also be reconciled with the prompt spectral distributions of GRB 100901A, which peak between optical and X-ray, if $\nu_{\rm opt} < \nu_{\rm c} < \nu_{\rm x}$. Then, a migration of the cooling frequency $\nu_{\rm c}$ ($\propto t^{-1/2}$; see, for example, Sari et al. 1998) might be hidden in the errors of the resulting $A_V^{\rm int}$. A spectral fitting of an absorbed power law to the late-time MASTER and 0.3–10 keV data provides $A_V^{\rm int} = 0.45 \pm 0.15$, lower than $A_V^{\rm int} = 0.8 \pm 0.1$ for the prompt fits (these values are for the SMC-type of extinction law; see Section 4.2). This could be a confirmation of the above suggestion, but a detailed discussion is beyond the aims of this paper.

In contrast, GRB 100906A exhibits no correlation between the optical and high-energy emission at 15–150 keV. We suggest that, in this case, the optical radiation originates at the front of the external shock, and the light curve shows a smooth conversion of a bow shock to a self-similar mode of the afterglow with a power decay $F_{\rm opt} \propto t^{-\alpha}$ with $\alpha = 1.08 \pm 0.01$ (Table 14; see also Kuvshinov et al. 2010).

A critical test for determining the site of the optical emission could be the observation of polarization. If radiation in the internal shock occurs in the ordered magnetic field, some polarization is expected (see, for example, Steele et al. 2009). This implies that the magnetic field coherence scale is larger than the size of the visible emitting region. Thus, a discovery of a considerable (>10 per cent) polarization of the optical radiation, correlating with the prompt γ-ray emission, would be strong evidence in favour of the optical radiation originating in the internal shock. Conversely, the afterglow radiation from the external shock occurs in the chaotic field of the ISM compressed by the shock, and should not have a considerable polarization (Gruzinov & Waxman 1999). A low degree of polarization of the optical light would rule out the presence of a large-scale ordered magnetic field in the emitting region (Mundell et al. 2007).

Fig. 4 shows our simultaneous observations of GRB 100906A with two orthogonal polaroids. The signals in the two channels are the same, with an accuracy of 0.5 per cent. The absence of the strong polarization is consistent with the picture of the different producing sites of the high-energy and optical radiation in GRB 100906A. However, we should note that the MASTER polarization observations of GRB 100906A were made with two optical tubes of one telescope. Such a mode of observations is restricted in the sense of giving definite information on the linear polarization (see Appendix A). The polarization filters are oriented differently in the celestial coordinate system at the telescopes of the MASTER-Net. A future observation of a suitable GRB by two MASTER telescopes should thus provide accurate polarization information. For the observations of GRB 100906A, we can infer that in the time interval from 100 s to ∼1 h the degree of linear polarization of the optical emission is less than 10 per cent with a probability of about 60 per cent (see Appendix A and Fig. A1). Full information about the inferred fractional linear polarization can be retrieved from Fig. A1. We note that the probabilities are obtained under a very conservative assumption that a source can have any fractional linear polarization from 0 to 100 per cent.

5.2 General spectral properties

In order to view the spectral characteristics of the observed GRBs at one glance, we construct in Fig. 12 a diagram of the optical flux density versus X-ray flux density at 3 keV, following Jakobsson et al. (2004). However, we do not plot the values extrapolated to the 11-h time mark, but rather the evolution for each GRB. Here, a spectral index β ($F_\nu \propto \nu^{-\beta}$) is shown by straight lines. Each optical observation is corrected for the Galactic extinction at a specific waveband using the NED Galactic Extinction calculator. As the intrinsic spectrum is not known a priori, we do not include a correction for the host extinction. The 3-keV flux densities are the best-fitting values obtained with an absorbed power-law model in the *Swift*/XRT energy band. For GRB 100902A, GRB 100905A and GRB 101020A, only the upper optical limits are shown.

The limit for GRB 100902A at 132–162 s shows that the burst was X-ray bright and very faint in the optical waveband at the time, possibly because of a large intrinsic extinction. Provided that $T_{90} = 429$ s (Stamatikos et al. 2010), the GRB is expected to have low $\beta_{\rm ox}$ at (0.3–0.4) T_{90}. This might be a 'dark' GRB, according to a classification by Jakobsson et al. (2004), bearing in mind its very prominent position on the diagram. GRB 100902A appears to

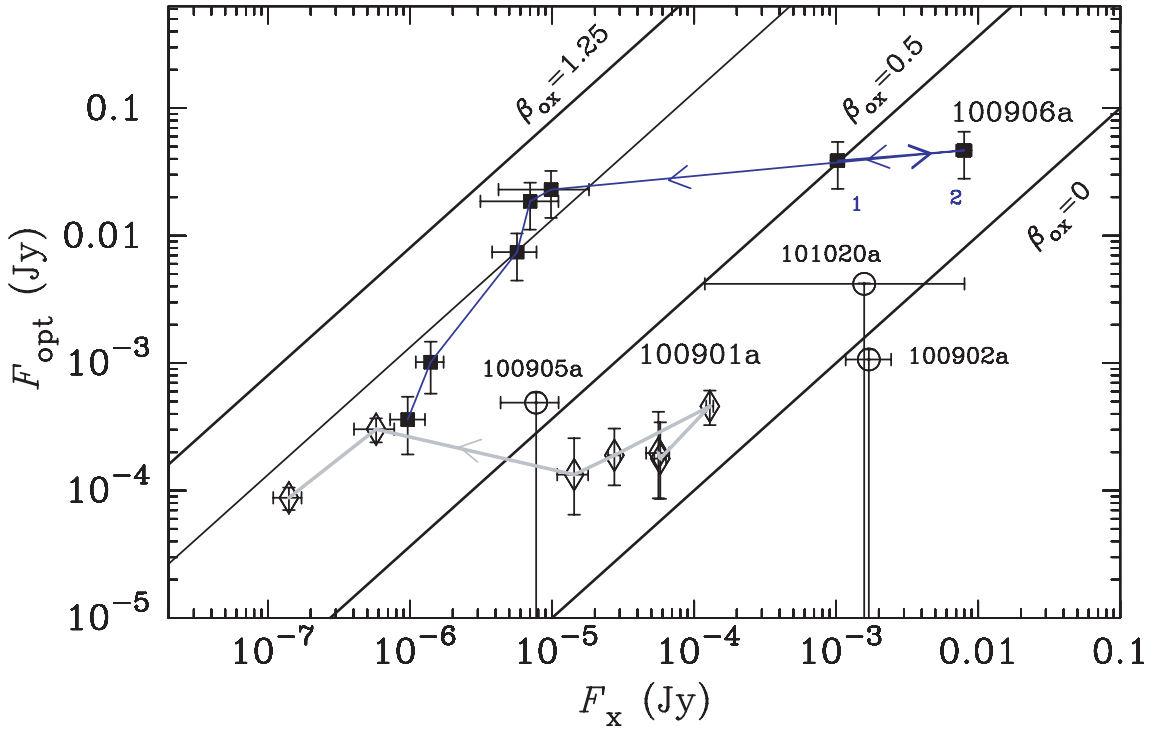

Figure 12. Diagram of the optical flux density versus X-ray flux density at 3 keV for five GRBs observed by MASTER in 2010 September and October. Each point represents a simultaneous observation in the optical and by *Swift*/XRT. The optical flux densities have been corrected for the Galactic extinction. Diamonds connected with a grey line show the evolution of GRB 100901A for eight time intervals of 193–233, 312–372, 387–467, 481–581, 595–715, 3800–4150, 27 000–28 500 and 102 800–121 500 s; squares connected by blue lines show the evolution of GRB 100906A for seven time intervals of 84–94 (point 1), 105–125 (point 2), 330–390, 410–480, 942–1112, 6000–7000 and 10 300–11 000 s. For GRB 100902A, GRB 100905A and GRB 101020A, only upper limits on optical flux density are given at post-trigger times 132–162, 150–180 and 106–126 s, respectively. When tracks are parallel to $\beta_{\rm ox} = {\rm const}$ lines, the optical flux density is emphatically correlated with the 3-keV flux density. We adopt Galactic extinctions $A_V = 1.037$ for GRB 100902A, $A_V = 0.191$ for GRB 100905A and $A_V = 0.051$ for GRB 101020A from the NED Extragalactic Calculator.

be darker than any of the GRBs of the sample of Jakobsson et al. (2004, see their fig. 1), with all of them being above the $\beta_{\rm ox} = 0$ line.

An anticorrelation between the excess absorption column densities and the redshifts of GRBs is expected because of the shift of the source rest-frame energy range below 1 keV out of the energy range observable with the XRT. Thus, Grupe et al. (2007) suggest a relation to estimate an upper limit on the redshift. From the late-time spectrum of GRB 100902A, an excess absorption column density of $\sim 2.8^{+0.6}_{-0.7} \times 10^{21}$ cm^{-2} is found, and an upper limit for $z \approx 3.2$ (substituting a lower value of $N_{\rm H}$ from equation 1 of Grupe et al. 2007). High redshifts are thought to be responsible for the darkness of GRBs, but the redshift obtained above is not high enough for this scenario (see, for example, Jakobsson et al. 2004, and references therein). However, the expression by Grupe et al. (2007) is inferred for non-dark GRBs and might be unapplicable. We also note that the analysis of Campana et al. (2010), using a cut-off power-law model, suggests a higher redshift of $z \sim 4.5$.

The MASTER observation of GRB 100905A was done at the time interval 150–180 s, which is much later than $T_{90} = 3.4$ s. It can belong to the class of intermediate duration GRBs (Horváth 1998, 2002; Mukherjee et al. 1998). At 150–180 s after the trigger, its XRT spectral slope is $\beta_{\rm x} = 0.2 \pm 0.2$. If the optical emission belongs to the same spectral distribution, this would explain its weakness, because the line $\beta_{\rm ox} = 0.2$ intersects the region of GRB 100905A on the diagram at $F_{\rm opt}$ values well below the optical limit.

GRB 101020A could not be observed by the *Swift*/XRT. The flux density at 3 keV for time $0.65 \times T_{90}$, where $T_{90} = 177$ s, is extrapolated from the BAT data and has considerable uncertainty, thus resulting in a wide area in Fig. 12. Nevertheless, the optical-to-X-ray flux ratio can be similar to that of GRB 100901A and GRB 100906A.

We see from Fig. 12 that the flux density ratios of GRB 100901A and GRB 100906A ultimately tend to the area between $\beta_{\rm ox} = 0.5$ and 1.25. This is consistent with the fireball model (e.g. Sari et al. 1998). The spectral slope ~ -1 at late times is consistent with the prediction for the slow-cooling regime for frequencies higher than the cooling frequency for electrons with the distribution of Lorentz factors $N(\gamma_e) \propto \gamma_e^{-p}$ with $p \gtrsim 2$.

The distinct prompt behaviour of GRB 100901A and GRB 100906A is evident in the diagram. We witness the optical and X-ray flux density correlation in GRB 100901A at the time of the last γ-ray pulse, together with an approximately constant spectral index. In GRB 100906A, during the γ-ray pulse, occurring about 100 s after the trigger, the 3-keV flux density undergoes a strong variation. The same can be said about the spectral indices in the XRT and BAT bands. However, the optical flux density is roughly at the same level. We note that the spectral fitting provides evidence that the prompt high-energy SED has a peak, which migrates from about 30 to 4 keV at times 80–130 s after $T0$ (see Section 4.1). It should be added that during those times the X-ray emission in the interval of 0.3–10 keV can be contributed by the two different sites

with proportions varying with time: one that is responsible for the γ-rays and one producing the optical photons.

5.3 Amati and Ghirlanda relations for GRB 100901A

The total duration BAT spectrum of GRB 100901A yields $E_{\rm iso} = 6.3 \times 10^{52}$ erg in the energy interval 1–10^4 keV in the rest frame. From the Amati relation (Amati 2006), we find the expected position of the energy distribution peak in the rest frame $E_{\rm p,i} = 230$ keV. Translated to the observer frame, this becomes $E_{\rm p} \sim 100$ keV. This does not contradict with the lower limit $E_{\rm p}^{\rm min} \sim 75$ keV, derived on the basis that no characteristic energy can be found from the spectral analysis of the BAT data, and the photon index of the power law is about -1.5.

The 0.3–10 keV light curve $\propto t^{-1.5}$ from 4×10^4 s to about 10^6 s when a possible steepening occurs. The MASTER W-band light curve enables only a rough evaluation of temporal index in the interval 3×10^4–3×10^5 s: it is decaying approximately as $\sim t^{-1.3}$ with just one late optical point at $\sim 10^5$ s. Using the tentative jet break time $\sim 10^6$ s, we obtain the opening half-angle of the jet $\sim$13 deg for the efficiency of converting the ejecta energy into γ-rays $\eta_\gamma = 0.2$ and the number density of the ambient medium $n = 3$ cm^2. Few jets are reported to have comparably wide angles (Ghirlanda, Ghisellini & Lazzati 2004). The corresponding collimation-corrected energy would be $E_\gamma = 1.7 \times 10^{51}$ erg. Using the Ghirlanda relation, this predicts $E_{\rm p,i} \sim 700$ keV, a value about three times higher than the prediction of the Amati relation.

We conclude that GRB 100901 is consistent with the Amati relation, if $E_{\rm p,i} \sim 230$ keV, but the Ghirlanda relation is hardly applicable.

5.4 Amati and Ghirlanda relations for GRB 100906A

By fitting the spectrum of GRB 100906A in the time interval 3–142 s with the Band function, Golenetskii et al. (2010) have derived values $E_{\rm peak} = 142^{+119}_{-60}$ keV and $E_{\rm iso} = (2.2 \pm 0.4) \times 10^{53}$ erg. The peak of the energy distribution in the rest frame is at $E_{\rm p,i} = (1+z) \times E_{\rm peak} = 387^{+324}_{-164}$ keV. The central values of $E_{\rm iso}$ and $E_{\rm p,i}$ are close to the Amati correlation $E_{\rm p,i} = 95 \times E_{\rm iso}^{0.49}$ (see fig. 2 of Amati 2006).

If we assume a jet break time of $t_{\rm b} = 51 \pm 4$ ks (see Section 4.4) and if we substitute the above $E_{\rm iso}$ into equation 1 of Ghirlanda et al. (2004) – where we assume the values of the efficiency of converting the ejecta energy into γ-rays $\eta_\gamma = 0.2$ and the number density of the ambient medium $n = 3$ cm^2 – we obtain the opening half-angle of the jet $\theta_{\rm j} = 3.31 \pm 0.08$ deg. Then, the collimation-corrected energy is $E_\gamma \sim (3.7 \pm 0.7) \times 10^{50}$ erg. This value, together with $E_{\rm p,i}$, agrees with the Ghirlanda relation $E_{\rm p,i} \simeq 480 (E_\gamma / 10^{51}\ {\rm erg})^{0.7}$ (see fig. 1 of Ghirlanda et al. 2004). This is particularly the case because of the large uncertainty in the observed $E_{\rm peak}$ value of GRB 100906A.

5.5 Long life of a central engine

Katz & Piran (1997) have suggested that the prolonged activity of the central engine could be the source of an extended afterglow. Later, this was considered to be an explanation for the plateaux on the X-ray light curves of some GRBs (e.g. Zhang & Mészáros 2001; Zhang et al. 2006; Liang, Zhang & Zhang 2007; Willingale et al. 2007; Lipunov & Gorbovskoy 2008). In particular, the sharp drops at late times on the light curves indicate that such variations are likely to be the result of some internal mechanisms (Troja et al. 2007; Zhang 2009). To account for the lasting activity of the central engine of GRBs, a model of a rapidly spinning, highly magnetized neutron star – a 'proto-magnetar' – formed as the result of a core collapse, has been proposed (see a review by Metzger 2010). Another object that can provide a long-term energy supply is a rapidly spinning, magnetized collapsed core with a mass exceeding the upper limit for a neutron star. Its fast rotation stops the collapse, and a quasi-stationary configuration is presumably formed at this stage; this is called a 'spinar' (Lipunova 1997; Lipunov & Gorbovskoy 2007). Before a collapse to a black hole is possible, enough angular momentum should be taken out from the system. The time required for angular momentum dissipation determines the duration of the central engine activity and depends on the magnetic field strength, as the energy and angular momentum losses are governed by the magneto-dipole mechanism.

Lipunov & Gorbovskoy (2008) proposed a set of one-dimensional equations to determine the evolution of a collapsing rotating magnetized core with the main relativistic effects taken into account. These equations describe the principal behaviour of both the proto-magnetar and the spinar. Solutions suggest two peaks in the release of energy: the first takes place when the dynamical collapse is halted by centrifugal or pressure forces, and the second is when the final contraction occurs. The peaks are separated by a plateau. Three exemplary solutions of the equations by Lipunov & Gorbovskoy (2008) are shown in Fig. 13. The first peak is set to occur at zero time, and this is not shown in detail. In the model, the first peak is evaluated on a dynamical time-scale and does not involve specific jet radiation mechanisms. If the first stage of a collapse finishes close to $r_{\rm g} = G M / c^2$, then the second peak is extinguished. The power of a proto-magnetar, defined by the pulsar dipole mechanism, approaches the t^{-2} law after the second peak. A power of a spinar always has a very sharp drop after the second peak. For each of the models in Fig. 13, the calculated power is multiplied by an arbitrary factor of 0.1.

Two curves with lower plateaux represent models with mass $M = 1.9\ {\rm M}_\odot$. They both vary as $\propto t^{-2}$ at late times. In the model

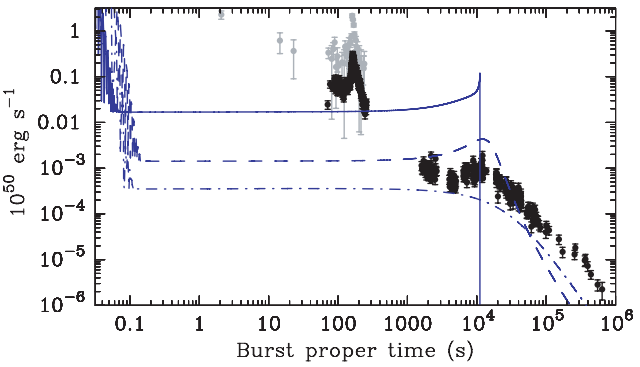

Figure 13. The energy release of a collapsing core is calculated following Lipunov & Gorbovskoy (2008). Points with bars are the observed 0.3–10 and 15–150 keV fluxes from GRB 100901A (Sakamoto et al. 2010b; Page & Immler 2010) translated to redshift 1.408. Three curves with plateaux represent numerical solutions for energy release rates, multiplied by 0.1, for cores of different mass and angular momentum. The dashed and dot-dashed lines are solutions for proto-magnetars of the same mass and with different angular momentum at the halt of the initial dynamical collapse that produced the first peak before the plateau. The first peak is referred to as time zero; the details of the first peak are of no relevance. The top solid line shows the solution for a collapsing core with such a mass that makes a collapse to a black hole inevitable. For specific parameters of the models, see Section 5.5.

with monotonic transition to a decay, a proto-magnetar forms with period $P = 2$ ms and a poloidal magnetic field $B \sim 4 \times 10^{14}$ G at $\sim 13\, r_g$. The middle plateau represents a newly born magnetar of higher angular momentum; the dynamical collapse halts at about $40\, r_g$ with $P = 5$ ms and $B \sim 7 \times 10^{13}$ G. The object contracts further, to $10\, r_g$, causing a spin-up to $P = 1.7$ ms and the dipole magnetic field amplification up to $\sim 10^{15}$ G. This specific evolution manifests itself as a bump at the end of the plateau. The solid curve shows a solution for a spinar with $M = 4\, M_\odot$. At the plateau, the dimensionless Kerr parameter $a_{\rm Kerr} = Jc/GM^2 = 3$, $P \sim 1$ ms, $B \sim 1.5 \times 10^{13}$ G, and the characteristic radius $15\, r_g$. The spike at the end is numerically solved and indicates the collapse to a black hole. The initial magnetic field strengths are chosen in order to obtain the characteristic time of a plateau $\sim 10^4$ s.

Both a spinar and a proto-magnetar can explain the long activity of GRBs. The law of temporal decay after the second peak (or after the end of a plateau) can be determined mainly by the processes in the jet and ambient media and, to a lesser degree, by the nature of the central object. The efficiency factor, which is set to 0.1 for Fig. 13, cannot be constrained in our general approach.

6 SUMMARY

The development of the MASTER-Net of optical robotic telescopes, which is coming into full operation over Russia, has been encouraged by the need for dense early observations of GRBs around the globe. Optical ground-based observations, with polarization measurements, are indispensable for revealing the nature of the central engine of GRBs. By observing simultaneously with several telescopes, the MASTER team plan to obtain optical linear polarization information as soon as possible after a GRB trigger, before γ-emission ceases. Our goal is to deliver full polarization information for GRBs in the optical band as soon as possible after the trigger time.

Here, we have presented some results from the MASTER-Net. During 2010, MASTER observed the five GRBs described in this paper. Optical transients were found for two bursts, GRB 100901A and GRB 100906A. A detailed analysis of these GRBs was carried out, based on MASTER data, data from the 1.5-m telescope at OSN and the 2.56-m NOT, as well as the publicly available data from the *Swift* mission.

The light curves and spectra of GRB 100901A and GRB 100906A suggest that the prompt optical emission has different origins. The correlation between the optical and high-energy light curves of GRB 100901A, as well as the results of the spectral fitting, favour the hypothesis of a common origin for the optical and high-energy spectra. During the γ-ray flare that started about 300 s after the trigger, the slope of the spectral distribution from the optical to 150 keV is close to $-1/2$. This is expected for synchrotron radiation at frequencies above the cooling and below the characteristic synchrotron frequency in the 'fast cooling' regime (see, for example, Sari & Piran 1999). The resulting values of the host optical extinction are consistent for the prompt fits and are similar to the values obtained by fitting an absorbed power law to the late-time spectral data. This means that the prompt optical points lie on the same spectral distribution that describes the γ- and X-ray data, which supports the hypothesis of their common production site and mechanism. The estimated ratio of the GRB host hydrogen column density $N_{\rm H}^{\rm int}$ to the total extinction $A_V^{\rm int}$ suggests that the host of GRB 100901A possesses a metal-to-dust ratio comparable to the level measured for the MW, SMC or LMC.

For GRB 100906A, there is no apparent correlation between the optical and 15–150 keV light curves. We suggest that, for GRB 100906A, the prompt optical radiation originates in a region different from the γ-ray production site, probably in a front shock. An analysis of GRB 100906A reveals that a spectral component, responsible for the γ-ray pulse at ~ 100 s after the trigger and for the downward migration of the X-ray peak on the spectral energy distribution, does not correlate with the optical emission at these times.

The signals in two orthogonal polarizations, measured by the MASTER telescope at Tunka from GRB 100906A, are found to be equal within 0.5 per cent. We calculate the probability distribution for the fractional linear optical polarization of GRB 100906A. We point out that future observations of a GRB by at least two MASTER telescopes should yield accurate polarization information.

The 0.3–10 keV light curve of GRB 100906A has a break around 14 h after the trigger. The X-ray spectral index (non-variable around the break) and the temporal slopes can be reconciled with the closure relations for the relativistic jet in the 'slow cooling' regime before the break and the spreading uniform jet after the break. It is not clear from the data in the R band if this break is achromatic. The estimated jet opening angle, 3.31 ± 0.08 deg, and collimation-corrected energy, $E_\gamma \sim (3.7 \pm 0.7) \times 10^{50}$ erg, imply that GRB 100906A follows the Amati relation and does not contradict the Ghirlanda relation. An analysis of the late-time spectra provides the upper limit on the optical extinction in the GRB host.

ACKNOWLEDGMENTS

We thank the referee for many useful comments. We are grateful to T. Piran for his help. We also thank K. Sokolovsky. We acknowledge Taka Sakamoto and Scott D. Barthelmy for the BAT data. This work was supported by the Ministry of Science of the Russian Federation (state contract no. 02.740.11.0249). ESG thanks the Foundation for Non-Profit Programmes 'Dynasty'. GVL is supported by the Russian Foundation of Fundamental Research, grant RFFI 09-02-00032. The research of JG, AJCT, JCT, MJ and RSR is supported by the Spanish programmes AYA2007-63677, AYA2008-03467/ESP and AYA2009-14000-C03-01. We are grateful to S. M. Bodrov for the ceaseless support of the MASTER-Net. This work made use of data supplied by the UK *Swift* Science Data Centre at the University of Leicester. This research has also made use of the NED, which is operated by the Jet Propulsion Laboratory, California Institute of Technology, under contract with the National Aeronautics and Space Administration. We have also used the publicly available results of the SDSS (http://www.sdss.org/). This research has made use of NASA's Astrophysics Data System.

REFERENCES

Abazajian K. N. et al., 2009, ApJS, 182, 543
Akerlof C. et al., 2000, ApJ, 532, L25
Amati L., 2006, MNRAS, 372, 233
Arnaud K. A., 1996, in Jacoby G. H., Barnes J., eds, ASP Conf. Ser. Vol. 101, Astronomical Data Analysis Software and Systems V. Astron. Soc. Pac., San Francisco, p. 17
Atwood W. B. et al., 2009, ApJ, 697, 1071
Barthelmy S. D. et al., 2010a, GRB Coord. Network, Circ. Service, 11218, 1
Barthelmy S. D. et al., 2010b, GRB Coord. Network, Circ. Service, 11233, 1
Beardmore A. P., Markwardt C. B., 2010, GRB Coord. Network, Circ. Service, 11244, 1
Butler N. R., Kocevski D., 2007, ApJ, 663, 407

Campana S., Starling R. L. C., Evans P. A., Sakamoto T., 2010, GRB Coord. Network, Circ. Service, 11195, 1
Chornock R., Berger E., Fox D., Levan A. J., Tanvir N. R., Wiersema K., 2010, GRB Coord. Network, Circ. Service, 11164, 1
de Ugarte Postigo A. et al., 2011, A&A, 525, A109
Evans P. A. et al., 2009, MNRAS, 397, 1177
Evans P. A. et al., 2010, A&A, 519, A102
Everett M. E., Howell S. B., 2001, PASP, 113, 1428
Gehrels N. et al., 2004, ApJ, 611, 1005
Ghirlanda G., Ghisellini G., Lazzati D., 2004, ApJ, 616, 331
Golenetskii S. et al., 2010, GRB Coord. Network, Circ. Service, 11251, 1
Gorbovskoy E. et al., 2010, GRB Coord. Network, Circ. Service, 11185, 1
Grupe D., Nousek J. A., vanden Berk D. E., Roming P. W. A., Burrows D. N., Godet O., Osborne J., Gehrels N., 2007, AJ, 133, 2216
Gruzinov A., Waxman E., 1999, ApJ, 511, 852
Hayes D. S., 1985, in Hayes D. S., Pasinetti L. E., Philip A. G. D., eds, Proc. IAU Symp. Vol. 111, Calibration of Fundamental Stellar Quantities. Kluwer, Dordrecht, p. 225
Horváth I., 1998, ApJ, 508, 757
Horváth I., 2002, A&A, 392, 791
Immler S. et al., 2010, GRB Coord. Network, Circ. Service, 11159, 1
Ivanov K. et al., 2010a, GRB Coord. Network, Circ. Service, 11161, 1
Ivanov K. et al., 2010b, GRB Coord. Network, Circ. Service, 11163, 1
Ivanov K. et al., 2010c, GRB Coord. Network, Circ. Service, 11216, 1
Jakobsson P., Hjorth J., Fynbo J. P. U., Watson D., Pedersen K., Björnsson G., Gorosabel J., 2004, ApJ, 617, L21
Jensen B. L. et al., 2001, A&A, 370, 909
Kalberla P. M. W., Burton W. B., Hartmann D., Arnal E. M., Bajaja E., Morras R., Pöppel W. G. L., 2005, A&A, 440, 775
Katz J. I., Piran T., 1997, ApJ, 490, 772
Kornilov V. G. et al., 2011, Exp. Astron., doi:10.1007/s10686-011-9280-z
Krushinski V. et al., 2010a, GRB Coord. Network, Circ. Service, 11182, 1
Krushinski V. et al., 2010b, GRB Coord. Network, Circ. Service, 11359, 1
Krushinski V. et al., 2010c, GRB Coord. Network, Circ. Service, 11361, 1
Kulkarni S. R. et al., 1998, Nat, 395, 663
Kuvshinov D. et al., 2010, GRB Coord. Network, Circ. Service, 11235, 1
Landi Degl'Innocenti E., Bagnulo S., Fossati L., 2007, in Sterken C., ed., ASP Conf. Ser. Vol. 364, The Future of Photometric, Spectrophotometric and Polarimetric Standardization. Astron. Soc. Pac., San Francisco, p. 495
Liang E-W., Zhang B-B., Zhang B., 2007, ApJ, 670, 565
Lipunov V., Gorbovskoy E., 2007, ApJ, 665, L97
Lipunov V. M., Gorbovskoy E. S., 2008, MNRAS, 383, 1397
Lipunov V. et al., 2010, Adv. Astron., 349171
Lipunova G. V., 1997, Astron. Lett., 23, 84
Lupton R., 2005, Transformations between SDSS magnitudes and UBVRcIc, http://www.sdss.org/dr7/algorithms/sdssUBVRITransform.html#Lupton2005
Markwardt C. B. et al., 2010, GRB Coord. Network, Circ. Service, 11227, 1
Marshall F. E. et al., 2010, GRB Coord. Network, Circ. Service, 11214, 1
Mészáros P., 2002, ARA&A, 40, 137
Mészáros P., Rees M. J., 1997, ApJ, 476, 232
Mészáros P., Rees M. J., 1999, MNRAS, 306, L39
Metzger B. D., 2010, in Stanford L. M., Green J. D., Hao L., Mao Y., eds, ASP Conf. Ser. Vol. 432, New Horizons in Astronomy: Frank N. Bash Symposium 2009. Astron. Soc. Pac., San Francisco, p. 82
Mukherjee S., Feigelson E. D., Jogesh Babu G., Murtagh F., Fraley C., Raftery A., 1998, ApJ, 508, 314
Mundell C. G. et al., 2007, Sci, 315, 1822
Page K. L., Immler S., 2010, GRB Coord. Network, Circ. Service, 11171, 1
Pei Y. C., 1992, ApJ, 395, 130
Pickles A., Depagne É., 2010, PASP, 122, 1437
Piran T., 2005, Rev. Mod. Phys., 76, 1143
Racusin J. L. et al., 2009, ApJ, 698, 43
Sakamoto T. et al., 2010a, GRB Coord. Network, Circ. Service, 11358, 1
Sakamoto T. et al., 2010b, GRB Coord. Network, Circ. Service, 11169, 1
Sakamoto T. et al., 2010c, GRB Coord. Network, Circ. Service, 11181, 1
Sanchez-Ramirez R., Tello J. C., Sota A., Gorosabel J., Castro-Tirado A. J., 2010, GRB Coord. Network, Circ. Service, 11180, 1
Sari R., Piran T., 1997, ApJ, 485, 270
Sari R., Piran T., 1999, ApJ, 520, 641
Sari R., Piran T., Narayan R., 1998, ApJ, 497, L17
Saxton C. J. et al., 2010, GRB Coord. Network, Circ. Service, 11357, 1
Schady P. et al., 2010, MNRAS, 401, 2773
Schlegel D. J., Finkbeiner D. P., Davis M., 1998, ApJ, 500, 525
Siegel M. H., Marshall F. E., 2010, GRB Coord. Network, Circ. Service, 11237, 1
Sota A., de Ugarte Postigo A., Castro-Tirado A. J., 2010, GRB Coord. Network, Circ. Service, 11220, 1
Stamatikos M. et al., 2010, GRB Coord. Network, Circ. Service, 11202, 1
Steele I. A., Mundell C. G., Smith R. J., Kobayashi S., Guidorzi C., 2009, Nat, 462, 767
Tanvir N. R., Wiersema K., Levan A. J., 2010, GRB Coord. Network, Circ. Service, 11230, 1
Tello J. C., Sanchez-Ramirez R., Sota A., Gorosabel J., Castro-Tirado A. J., 2010, GRB Coord. Network, Circ. Service, 11196, 1
Tody D., 1993, in Hanisch R. J., Brissenden R. J. V., Barnes J., eds, ASP Conf. Ser. Vol. 52, Astronomical Data Analysis Software and Systems II. Astron. Soc. Pac., San Francisco, p. 173
Troja E. et al., 2007, ApJ, 665, 599
Vestrand W. T. et al., 2005, Nat, 435, 178
Vestrand W. T. et al., 2006, Nat, 442, 172
Willingale R. et al., 2007, ApJ, 662, 1093
Winkler C. et al., 2003, A&A, 411, L1
Zhang X-H., 2009, Res. Astron. Astrophys., 9, 213
Zhang B., Mészáros P., 2001, ApJ, 552, L35
Zhang B., Mészáros P., 2004, Int. J. Mod. Phys. A, 19, 2385
Zhang B., Fan Y. Z., Dyks J., Kobayashi S., Mészáros P., Burrows D. N., Nousek J. A., Gehrels N., 2006, ApJ, 642, 354

APPENDIX A: ESTIMATING THE DEGREE OF LINEAR POLARIZATION FROM OBSERVATIONS USING TWO FIXED POLARIZING FILTERS

Observations of the bright GRB 100906 have been made with just one telescope that is able to provide polarization measurements (the MASTER telescope at Tunka). Generally, if an observation is made with only two polarizing filters at a single set of positions, only an estimate of the degree of linear polarization can be obtained.

Here, we assume zero circular polarization. Let $P_{\rm L}$ be the fraction of linearly polarized radiation and let θ be the angle of maximum polarization (i.e. the angle between the x-axis of the reference system and the segment that a polarization ellipse degenerates into for the case with zero circular polarization; see, for example, Landi Degl'Innocenti, Bagnulo & Fossati 2007). Then, $P_{\rm L} = \sqrt{P_Q^2 + P_U^2}$, where $P_Q = Q/I$, $P_U = U/I$ and I, Q and U are the first three Stokes parameters; I is the total intensity with no polarization filter interposed (in this appendix, we do not consider colour filters).

To derive the value of $P_{\rm L}$, we need to perform observations with filters for linear polarization positioned at three angles (e.g. at 0°, 45° and 90° with respect to the reference direction). We have two orthogonal filters at each of the MASTER-II telescopes; thus, if such a telescope observes alone, only a lower limit on $P_{\rm L}$ can be deduced. If this lower limit is a virtual zero, there is still some probability that the actual linear polarization is substantial.

Let I_1 and I_2 be the signals of the detector with filters at 0° and 90° interposed. Then, a value $D = (I_1 - I_2)/(I_1 + I_2)$ can be calculated, which is expressed as follows:

$$D = P_{\rm L} \cos 2\theta. \quad \text{(A1)}$$

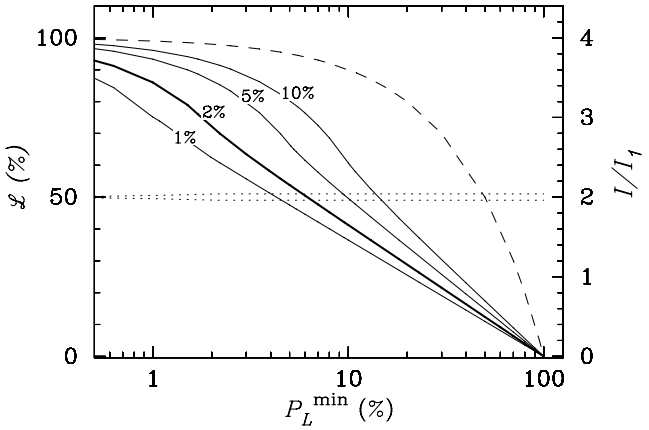

Figure A1. Left axis: likelihood $\mathcal{L}(P_{\rm L} \geq P_{\rm L}^{\rm min} \mid I_1 \approx I_2)$, where $I_{1,2}$ are the signals from two orthogonal polarizing filters, $P_{\rm L}$ is an unknown fractional linear polarization of a source and $P_{\rm L}^{\rm min}$ is a value plotted along the x-axis. The several likelihood functions are plotted as solid curves marked with the values of $\sigma_{\rm p}$, the known relative error between the measurements with two orthogonal polarizing filters. The dashed line shows the probability that an unobserved source has $P_{\rm L} \geq P_{\rm L}^{\rm min}$ under the prior hypothesis that a source has no preference for any degree of linear polarization. Right axis: the ratio of the total intensity I to the measured signal I_1 for $|D| < \sigma_{\rm p} = 2$ per cent. Its limits are shown by the double dotted line.

If the value of D differs from zero ($|D|$ is greater than the relative error $\sigma_{\rm p}$ between measurements with two differently positioned filters), a certain amount of linear polarization is present in the light with a lower estimate for it: $P_{\rm L}^{\rm min} = |D|$, calculated as if a filter is interposed at angles 0° or 90° with respect to the direction of the polarization plane of the incident light.

If the module of D is less than $\sigma_{\rm p}$, then formally we have zero as a minimum estimate for the degree of linear polarization. A hundred per cent linear polarization is also possible in this case, if a filter is accidentally positioned so that a source's polarization plane is inclined by 45° to it. This possibility can be numerically evaluated by considering the total range of filter positions that would result in a value of $|D| < \sigma_{\rm p}$. Substituting $D = \sigma_{\rm p}$ and $\theta = \pi/4 + \delta\theta/2$ in equation (A1), for any preset value of $P_{\rm L}$, we obtain a value of the allowable interval $\delta\theta$. Because our configuration consists of two orthogonal filters, the source polarization plane should be in either of the four intervals $\delta\theta$ around angles $N \times \pi/4$, where $N = 1$, 2, 3 and 4. Thus, a source with linear polarization degree $P_{\rm L}$ yields the value $|D| < \sigma_{\rm p}$ with probability $4\delta\theta/2\pi$. Now, we can calculate the conditional probability of a source with observed $|D| < \sigma_{\rm p}$ to have a particular degree of linear polarization $P_{\rm L}$ using the Bayes theorem. We make a conservative assumption that a source can have any fractional linear polarization from 0 to 100 per cent. From this, the likelihood function $\mathcal{L}(P_{\rm L} > P_{\rm L}^{\rm min} \mid I_1 \approx I_2) = \mathcal{L}(P_{\rm L} > P_{\rm L}^{\rm min} \mid |D| < \sigma_{\rm p})$ can be derived, where $I_1 \approx I_2$ is a realized event, $P_{\rm L}$ is the actual fractional linear polarization of a source and $P_{\rm L}^{\rm min}$ is some value of it.

The probability that the actual linear polarization of a source exceeds value $P_{\rm L}$ is shown in Fig. A1. Thus, for example, if no difference between I_1 and I_2 is registered in the measurements with 2 per cent error, there is a 50 per cent chance that a source has a linear degree of polarization greater than $\approx$6 per cent.

Accordingly, the total intensity from the source is greater than the observed $I_1 \approx I_2$. We can see from Fig. A1 that in observations with $|D| < \sigma_{\rm p}$, the total intensity is always greater by about the same factor (twice) than measured I_1. This can be seen by considering the expression for the signal from one polarizer: $I_1 = I(1 - P_{\rm L})/2 + I\,P_{\rm L}\cos^2\theta$. For small $P_{\rm L}$, the light behaves as unpolarized, and for large $P_{\rm L}$ the allowable interval $\delta\theta$ approaches zero and $\theta \approx \pi/4$.

SUPPORTING INFORMATION

Additional Supporting Information may be found in the online version of this article:

Table 1. Photometry of GRB 100901A by MASTER: *R*, unfiltered *W*, *I* and *V*.

Table 4. Photometry data for GRB 100906A by MASTER in the unfiltered band with two orthogonal polarizing filters.

Table 5. *UBVRI* photometry for GRB 100906A obtained by the OSN telescope.

Table 8. Stars from the SDSS-DR7 used as standard stars for GRB 100901A.

Table 9. Standard stars used for the photometry of GRB 100906A.

Please note: Wiley-Blackwell are not responsible for the content or functionality of any supporting materials supplied by the authors. Any queries (other than missing material) should be directed to the corresponding author for the article.

This paper has been typeset from a TEX/LATEX file prepared by the author.